Available online at www.sciencedirect.com
ScienceDirect
Icarus 193 (2008) 139–157
ICARUS
www.elsevier.com/locate/icarus

Derivation of martian surface slope characteristics from directional thermal infrared radiometry

Joshua L. Bandfield *, Christopher S. Edwards

School of Earth and Space Exploration, Arizona State University, Tempe, AZ 85281-6305, USA

Received 27 February 2007; revised 29 June 2007

Available online 15 September 2007

Abstract

Directional thermal infrared measurements of the martian surface is one of a variety of methods that may be used to characterize surface roughness and slopes at scales smaller than can be obtained by orbital imagery. Thermal Emission Spectrometer (TES) emission phase function (EPF) observations show distinct apparent temperature variations with azimuth and emission angle that are consistent with the presence of warm, sunlit and cool, shaded slopes at typically ∼0.1 m scales. A surface model of a Gaussian distribution of azimuth independent slopes (described by θ-bar) is combined with a thermal model to predict surface temperature from each viewing angle and azimuth of the TES EPF observation. The models can be used to predict surface slopes using the difference in measured apparent temperature from 2 separate 60–70° emission angle observations taken ∼180° in azimuth relative to each other. Most martian surfaces are consistent with low to moderate slope distributions. The slope distributions display distinct correlations with latitude, longitude, and albedo. Exceptionally smooth surfaces are located at lower latitudes in both the southern highlands as well as in high albedo dusty terrains. High slopes are associated with southern high-latitude patterned ground and north polar sand dunes. There is little apparent correlation between high resolution imagery and the derived θ-bar, with exceptions such as duneforms. This method can be used to characterize potential landing sites by assuming fractal scaling behavior to meter scales. More precisely targeted thermal infrared observations from other spacecraft instruments are capable of significantly reducing uncertainty as well as reducing measurement spot size from 10s of kilometers to sub-kilometer scales.

Keywords: Mars, surface; Infrared observations; Photometry

1. Introduction

The morphology of planetary surfaces is well documented by imaging systems on orbital spacecraft, but is limited in resolution to meter and (more often) greater scales. With the exception of a limited number of lander missions, it is not possible to use imaging systems to obtain a clear picture of sub-meter scale surface morphologies. Identification of these morphologies is important for understanding surface processes such as regolith/soil formation, dust mantling, rock generation and migration, and near-surface ice related processes. In addition, understanding the surface character at meter and smaller scales is crucial for characterizing and evaluating the safety and traffica-bility of potential landing sites for future spacecraft.

A number of techniques have been developed and used to gain insight into the sub-meter scale morphology of Mars and other planetary surfaces. These include use of photometric (e.g. Wagner, 1967; Hapke, 1984; Helfenstein, 1988; McEwen, 1991; Shepard and Campbell, 1998; Mushkin and Gillespie, 2006), laser altimeter pulse width (e.g. Garvin et al., 1999; Neumann et al., 2003), and radar measurements (e.g. Hagfors, 1968; Harmon et al., 1999; Campbell, 2001) to define surface slopes and roughness. In addition, surface temperature measurements have been used to derive surface roughness, particle size, and rock abundance of surfaces (e.g. Sinton, 1962; Spencer, 1990; Kieffer et al., 1977; Christensen, 1986). These methods provide quantitative information about the surface morphology that would otherwise be unobtainable via traditional imaging methods. Surface roughness is often defined in terms of the distribution of surface slopes as will be the case here. Depending on the measurement technique, roughness can

* Corresponding author. Fax: +1 480 965 1787.
E-mail address: joshband@asu.edu (J.L. Bandfield).

0019-1035/$ – see front matter
doi:10.1016/j.icarus.2007.08.028

also be defined by other means such as a range of elevations or the distribution of rocks.

A large amount of work has been done to account for and derive surface roughness at greater than sub-mm scales from the photometric function of a surface (e.g. Smith, 1967; Wagner, 1967; Hapke, 1984; Helfenstein, 1988; McEwen, 1991; Shepard and Campbell, 1998; Helfenstein and Shepard, 1999). Much of the behavior of the photometric function of a surface is due to microscopic and optical properties of the surface materials (e.g. Hapke, 1981; Shkuratov et al., 1999). However, macroscopic roughness where optical effects are treated geometrically also has significant influence on the photometric function (explaining, for example, the magnitude of limb darkening; Hapke, 1984). Because the roughness of a surface is typically reduced with increasing scale, photometric roughness is dominated by surface features less than a few cm in size (Helfenstein and Shepard, 1999). Under certain conditions, larger scales may be characterized if roughness properties at smaller scales are assumed to be invariant throughout a region (Mushkin and Gillespie, 2006).

Martian surface roughness characteristics at centimeter to meter scales can be obtained by telescopic radar observations of a variety of wavelengths (e.g. Harmon and Ostro, 1985; Muhleman et al., 1991; Simpson et al., 1992; Harmon et al., 1999; Golombek et al., 1999; Campbell, 2001). Observations have given estimates of rock abundances and distributions for a variety of surfaces (Golombek and Rapp, 1997; Baron et al., 1998; Golombek et al., 2003a; Campbell, 2001). Other studies have mapped surface roughness characteristics for major portions of the planet (e.g. Harmon et al., 1999). These studies have located extremely high radar return terrains, such as those associated with polar caps and the younger lava flows near the Tharsis and Elysium volcanoes. Anomalously low radar return regions have also been identified, such as the "stealth" region near southern Amazonis Planitia. These measurements give an indication of both the roughness of the surface terrain as well as the character of buried objects, such as rocks, that would serve as efficient scatterers.

Another method for determining surface roughness characteristics is by measuring the pulse width of laser altimeter return signals. This method has been applied to Mars Orbiter Laser Altimeter Data (MOLA) to gain insight into the vertical distribution of surfaces within the 75 m footprint of the laser pulse (e.g. Garvin et al., 1999; Neumann et al., 2003). With most of the planet sampled, Neumann et al. (2003) found that much of the martian surface has a root mean squared (RMS) roughnesses (i.e. the distribution of elevations within the MOLA footprint) of <3 m. The MOLA data are limited to RMS roughnesses of >1 m (Neumann et al., 2003). Slopes may also be obtained from differences in elevation between separate laser pulse measurements (e.g. Anderson et al., 2003). These determinations are limited to scales larger than $\sim$300 m, however.

Sub-pixel surface morphology information may also be inferred from the thermophysical properties of the surface. Both rock abundance determination (e.g. Christensen, 1986) and thermal inertia (e.g. Kieffer et al., 1977; Mellon et al., 2000) properties can be used to infer the presence of rocks on the martian surface. While these methods are not directly affected by the actual roughness of the surface, the presence of high thermal inertias and high rock abundances has accurately predicted the presence or absence of rough, blocky terrains (Christensen, 1986; Golombek et al., 1999).

A limited amount of work has been documented regarding the derivation of surface roughness properties from directional thermal infrared measurements (Jakosky et al., 1990). However, measurements across an object and whole disk measurements have been used to infer the surface roughness of the Moon and other airless bodies such as asteroids (e.g. Sinton, 1962; Spencer, 1990; Johnson et al., 1993; Jämsä et al., 1993). Much of this work has had a focus of producing a unitless parameter to correct for surface roughness effects (i.e. for radiometric diameter determination) rather than investigation of the sub-pixel surface morphology from the measurements. These measurements are sensitive to surface features of greater than several centimeters.

In this paper, we describe a technique for determining surface slope characteristics from targeted thermal infrared measurements on Mars. Emission phase function (EPF) measurements from the Thermal Emission Spectrometer (TES) onboard the Mars Global Surveyor (MGS) spacecraft are used in combination with surface and thermal models to infer roughness and slope characteristics of the martian surface. This work is largely a proof-of-concept with a limited application to the TES dataset. This demonstrates that useful surface roughness information may be obtained from specialized measurements from other Mars spacecraft instruments such as the Mars Climate Sounder (MCS) on the Mars Reconnaissance Orbiter and the Thermal Emission Imaging System (THEMIS) on the Mars Odyssey spacecraft.

2. Methods and data

2.1. Overview

The proportion of sunlit versus shaded surfaces in the field of view (FOV) is dependent on the viewing azimuth and elevation relative to the surface and the azimuth and elevation of the Sun. For example, when viewing a surface from the same azimuth as the Sun relative to the surface, a greater proportion of warm, sunlit surfaces comprise the FOV than if viewing a surface from an azimuth 180° away from the solar azimuth (Fig. 1). As a result, a surface will appear warmer or colder depending on the viewing azimuth and the magnitude of the effect is generally greater with increasing emission angles (Jakosky et al., 1990). This anisothermal effect is dependent on the magnitude of slopes present on the surface because of two factors: (1) High slope angles result in a large range of temperatures within the FOV. (2) High slope angles also cause a large change of the proportion of warm versus cold surfaces in the FOV as a function of viewing angle and azimuth.

There are three basic components that are integrated in the surface slope determination: (1) Multiple emission angle thermal infrared observations of a surface (specifically, TES EPF sequences are used here). These observations are corrected for

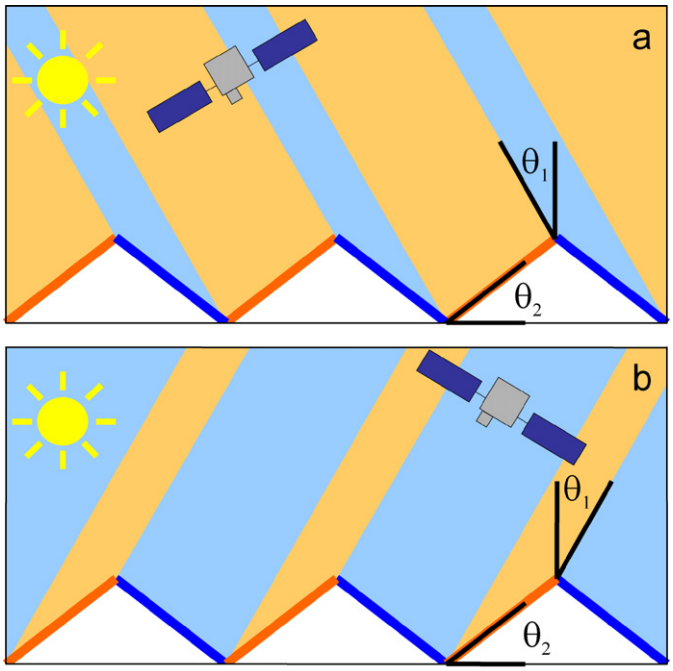

Fig. 1. Schematic displaying the change in contributions of sunlit versus shaded slopes to the spacecraft field of view. When viewing a surface from the same azimuth as the Sun (a), more sunlit surfaces are in the FOV and the surface will appear warmer. When viewing from an azimuth 180° from the Sun (b), the surface will appear cooler. The intensity of the effect is dependent on emission angle of the observation (θ_1) and the slope of the surfaces (θ_2).

atmospheric effects and are then reduced to a simple parameter for comparison to modeled data. (2) A thermal model is used to predict the surface temperature at various slopes and azimuths. (3) A surface model is used to provide a realistic distribution of slopes. Each of these three components are described in detail separately in Sections 2.2 through 2.4.

The three components (data, thermal model, and surface model) are integrated in order to determine the surface slope properties (described in Section 2.5). The thermal model and surface model are combined to predict the measured radiance from the known observation geometries for a variety of slope distributions. The measured radiance is then compared to the predicted radiance to retrieve the slope distribution that provides the best fit to the predicted radiance.

2.2. TES dataset

2.2.1. TES instrument description

The TES instrument is a Fourier transform Michelson interferometer (~6–50 μm) with co-aligned thermal (5–100 μm) and visible (0.3–3 μm) bolometers. Each detector in a 3 by 2 array has an 8 mrad instantaneous field of view with a 1.8 s integration time. This results in a 3 × ~8 km footprint from the ~380 km MGS mapping orbit with the elongation due to smear from the lack of image motion compensation. A pointing mirror allows for viewing of the surface, limb, and space in the orbital plane.

This study utilizes the thermal bolometer measurements because of their high signal to noise ratio and accuracy (Christensen et al., 2001), their relative simplicity, and many observations were acquired after the spectrometer was turned off in 2005 (to prevent further degradation of the internal neon lamp used for processing of the interferometer data). Initial use of spectrometer data provided similar results as those presented here from the broadband thermal bolometer measurements.

2.2.2. EPF dataset description

TES EPF observations have been utilized in several studies to derive surface emissivities and atmospheric aerosol properties (Bandfield and Smith, 2003; Clancy et al., 2003; Wolff and Clancy, 2003). All EPF observations are approximately symmetrical about a nadir observation and consist of 3 to 49 separate pointing angles. Because pointing capabilities are limited to the plane parallel to the spacecraft along-track direction, planetary rotation causes an east–west offset between the surface footprints of each pointing angle observation. The magnitude of this offset (which could have been compensated by a slight yaw of the spacecraft) is proportional to the cosine of the latitude, with nearly no effect at the poles and the greatest effect at the equator (Bandfield and Smith, 2003).

EPF observations were typically collected once per orbit on the daytime side of Mars throughout the MGS primary and extended missions. Most observations were targeted at fixed latitude intervals and random longitudes from 85° S to 85° N to document atmospheric phenomena. Several dozen EPF observations were targeted specifically for this study within the 65–72° N latitude range designated for the potential Mars Scout Phoenix spacecraft landing sites. Unfortunately, contact was lost with MGS before most of the observations planned for this study could be acquired. Observations were limited to those with relatively warm surface temperatures (>210 K) and high angles of solar incidence (>40°). Under these constraints, 4545 separate observations were acquired by the TES investigation.

Within each EPF observation, the data were restricted to 60–70° (typically ~65°) emission angles. Three to five separate measurements were acquired at each pointing angle for each detector and these are averaged to produce a single apparent brightness temperature. Each EPF observation is thus reduced to two apparent brightness temperatures acquired at the same ~65° emission angle and a difference of ~180° in azimuth from each other. The two brightness temperature measurements have a geometry that is symmetrical about the nadir observation (Fig. 1). The difference between the two temperatures (T_{diff}) is the fundamental measurement that is compared to the models discussed below.

The 60–70° emission angles maximize the difference in the relative contributions of sunlit and shaded slopes to the FOV while avoiding the severe atmospheric effects present with large atmospheric path lengths present at emission angles >70° (Bandfield and Smith, 2003). Lower emission angle observations could also be used to constrain surface slope characteristics. However, lower emission angles have a much reduced change in apparent temperature and were found to add little useful information beyond the 60–70° emission angle observations (55° emission angle observations have roughly half the effect of 65°). The symmetrical nature of the observation and the fo-

cus on the apparent temperature difference (discussed in detail below) largely cancels most uncertainties present. This includes uncertainties in the surface temperatures predicted by the thermal model and uncertainties in the correction for atmospheric effects on the measured data.

The final footprint size for each EPF observation is roughly a 20 by 80 km spot because of the greater distance to the surface from the 60–70° emission angle observations and averaging of multiple measurements within each pointing angle observation. Additionally, planetary rotation during the time between the two pointing angle observations results in a east–west offset of up to 120 km depending on the latitude of the observation. This is discussed in detail in Section 3.2.

2.2.3. Derivation of atmospherically corrected apparent surface temperatures

Uncertainties in the correction for atmospheric effects on T_{diff} are relatively small because the difference in temperature, rather than absolute temperature, is used and because of the symmetrical nature of the observation (with similar atmospheric path lengths). However, the radiative effect of a constant atmosphere on surfaces of different apparent temperatures is different, necessitating a correction for its effects. The atmosphere absorbs and scatters surface radiance and emits its own radiance into the instrument FOV. If the temperature of the atmosphere is identical to the observed surface, the magnitude of these effects on the measured radiance is close to zero. The magnitude of the atmospheric effects increases with increasing temperature contrast between the surface and the atmosphere. For example, a typical EPF observation of a warm surface under a relatively cold atmosphere will display a T_{diff} of ∼5–10 K between the two complimentary 65° emission angle observations. The surface–atmosphere temperature contrast and thus the atmospheric effects will be larger for the warmer observation. Under these conditions, T_{diff} is somewhat subdued (by typically ∼20%) over what would be measured with a correction for atmospheric effects.

It is also important to correct for atmospheric effects because of the non-linear nature of Planck radiance versus temperature. With a relatively warm surface and cold atmosphere (typical of a local time of 1400 with a low atmospheric dust opacity), the apparent temperatures will be colder by 10–15 K than would be measured without atmospheric effects. As an example, the same radiance difference measured from two separate EPF observations near 220 and 235 K will result in a 7% larger T_{diff} for the colder observation.

Atmospheric effects are corrected in the data for both gas and dust aerosol absorptions using a radiative transfer model similar to that described by Bandfield and Smith (2003). All data were corrected assuming a nominal, relatively clear period ($\tau_{\text{dust}} = 0.10$ at 9 μm) with a relatively cold atmosphere (170 K at 0.5 mbar) characteristic of northern hemisphere high latitude summer conditions. The effects of variable atmospheric conditions are discussed below.

The modeled difference between surface emitted radiance and radiance as measured at the top of the atmosphere is added to the measured bolometric radiance at each angle of the EPF observation. The corrected bolometric radiance is converted to a corrected apparent brightness temperature using a lookup table of calculated bolometric Planck radiances.

2.3. Thermal model description

The temperature of any given surface can be predicted using a thermal model and input parameters (e.g. latitude, season, elevation, local time, albedo, atmospheric dust opacity, thermal inertia, slope, and azimuth). We use the KRC thermal model (H.H. Kieffer, in preparation) to predict surface temperatures. This model has been used by a number of researchers (e.g. Titus et al., 2003; Fergason et al., 2006) and allows for customization of a wide variety of parameters such as changes in subsurface thermophysical properties and atmospheric aerosol properties. Results compare favorably (Fergason et al., 2006) with a related thermal model that has been used to derive surface thermal inertias from TES data (Jakosky et al., 1990; Mellon et al., 2000; Putzig et al., 2005).

Thermal inertias derived from daytime temperature measurements are not as accurate as those derived from nighttime temperature measurements because of the relatively high influence of slope, albedo, and atmospheric aerosol characteristics and their associated uncertainties on daytime surface temperatures. For this work, it is the difference in temperature based on slopes that is the important factor. This difference has a lower uncertainty than the predicted absolute daytime temperature because the uncertainties inherent in the modeling of daytime temperatures affect the surfaces in a consistent manner. The effects of uncertainties in the thermal modeling will be discussed below.

2.4. Surface model description

A number of models for the description of the macroscopic surface roughness have been developed and compared for predicting and interpreting the character of planetary surfaces (e.g. Hagfors, 1964; Beckmann, 1965; Smith, 1967; Hapke, 1984; Spencer, 1990; Shepard et al., 1995; Shepard and Campbell, 1998; Helfenstein and Shepard, 1999; Shepard et al., 2001). However, many of these models have been developed with a focus on simply accounting for surface roughness with the measurement technique to derive other properties (e.g. Smith, 1967; Hapke, 1984; Spencer, 1990). These models have been subsequently evaluated using visible photometry, thermal, and radar datasets with respect to geological interpretation of surface roughness characteristics (Helfenstein, 1988; Shepard et al., 1995; Shepard and Campbell, 1998; Helfenstein and Shepard, 1999).

We chose to use the θ-bar parameter described by Hapke (1984) as a model for surface slopes (Fig. 2). This model is based on a Gaussian distribution of slopes along a surface cross-section that is expanded to a full three dimensional surface assuming that the azimuths of slopes are random. This model is independent of length scales and can be described using a single parameter. While this simplicity is well suited for the derivation of surface slope distributions from the data, it is not

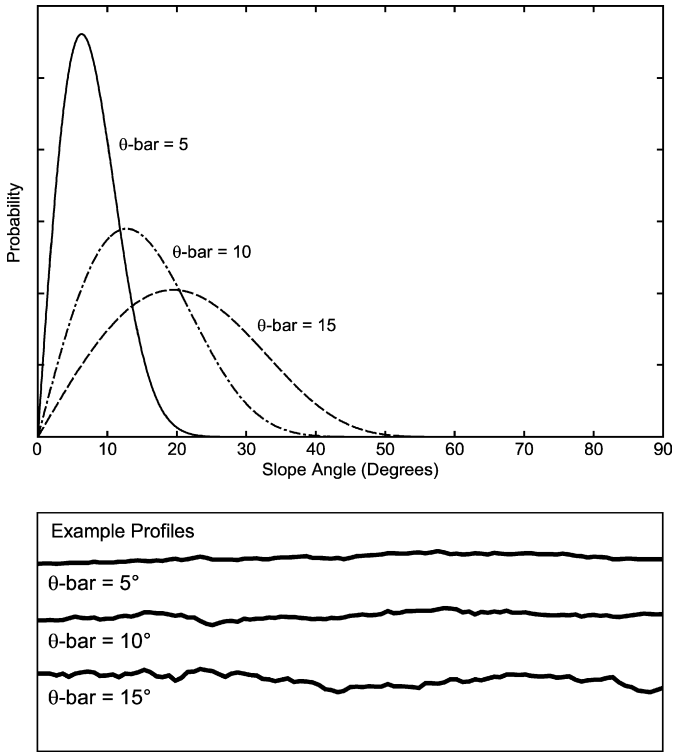

Fig. 2. Top: Azimuth independent Gaussian slope distributions for several values of (azimuth dependent) mean slope angle (θ-bar). Bottom: Example cross sectional profiles for the θ-bar distributions plotted above.

adequate for geological interpretation of surfaces as it does not account for the scale at which the roughness occurs. In addition, Kirk et al. (2003) noted a higher occurrence of extremely high slopes for martian surfaces at 12 m scales than would be expected from a Gaussian distribution. These deviations occur for $\sim$1% of the surfaces and would have little effect on the measurements. This will have a large effect on the estimation of the relative occurrence of large slopes with probabilities of $<$1%.

The scaling of surface roughness with length is well documented for natural surfaces and can be well described by fractals (Mark and Aronson, 1984; Shepard et al., 1995; Helfenstein and Shepard, 1999). This generally requires two parameters; RMS roughness at a specified scale and the Hurst exponent, which describes how the roughness changes with scale. Derivation of fractal parameters from the thermal infrared data is inappropriate because there is no inherent scaling information present in the apparent temperature measurements. However, we will compare the θ-bar derived from the TES data to equivalent fractal models in the discussion section below following the results of Shepard and Campbell (1998) and Helfenstein and Shepard (1999).

The θ-bar surface model used in this work produces an array of slopes (2° intervals) and azimuths (20° intervals) along with a weighting to define the contribution of each slope/azimuth combination to the measurement. This weighting is based on the Gaussian statistics of the θ-bar parameter and the projection of each surface to a plane normal to the viewing elevation and azimuth of the measurement. Self shadowing of surfaces is accounted for by applying a weighting of zero to all surfaces where the observing spacecraft is below the local horizon of the individual surface facet. It is assumed that surfaces blocked from the view of the observing spacecraft by other surfaces are of a random nature and do not need to be explicitly accounted for (e.g. Hapke, 1984).

2.5. Integration of data and models

It is the integration of the measured radiance with the surface and thermal models that allows for the retrieval of quantitative slope information. This is done by the following steps: (1) The measured T_{diff} is calculated from the atmospherically corrected TES bolometer EPF measurements. (2) The thermal model is used to predict surface temperatures for each slope/azimuth used in the surface model. (3) The modeled surface temperatures are converted to integrated radiance, weighted by the surface model slope and azimuth distributions. The modeled surface radiances are also weighted by their contribution to the spacecraft FOV for each EPF observation elevation and azimuth. (4) The weighted radiance is converted back into an apparent brightness temperature for each viewing elevation/azimuth in the TES EPF observation and the predicted T_{diff} is calculated. (5) A simple lookup table of θ-bar versus predicted T_{diff} is constructed for θ-bar values of 4–28° at 4° intervals. (6) Finally, θ-bar is obtained by interpolation of the measured T_{diff} (from step 1) using the predicted θ-bar/T_{diff} lookup table.

3. Sensitivities and uncertainties

Each aspect of the measurements and models described above has an associated set of uncertainties and sensitivities. We separate these into four sections based on uncertainties in the data and models and the scale of sensitivity to surface features. Sections 3.1 and 3.2 discuss the uncertainties in the measured T_{diff} from TES EPF observations. This includes the uncertainties in the derivation of surface temperature as well as the uncertainties due to the smearing out of the measurement footprint due to planetary rotation. Section 3.3 discusses the uncertainties in predicted T_{diff} from the thermal and surface model, such as those due to assumed atmospheric and surface properties. Section 3.4 discusses the sensitivity of this technique to the scale of surface features through 2-dimensional thermal modeling.

3.1. Surface temperature derivation sensitivities

A dominant effect on the bolometer surface temperature measurements is atmospheric gas and aerosol absorptions, which typically cause a 10–15 K underestimate of surface temperature under conditions with a warm surface and cold atmosphere. As discussed above, even though atmospheric effects largely cancel in the determination of T_{diff}, it is still necessary to account for these effects. Using again the example of the TES EPF measurements from Orbit Counter Keeper (OCK) 9938, we can gain insight into the effects of the atmosphere on θ-bar determination (Table 2).

The T_{diff} determined from (atmospherically) uncorrected data is 4.5 K and is 5.1 K for corrected data assuming the atmospheric characteristics described above. This causes a difference of 0.6° in the derived θ-bar. Increasing atmospheric temperature by 20 K and tripling the dust opacity (to 0.45 at 9 μm), increases T_{diff} to 1.4 K, resulting in a difference of 1.3° in the derived θ-bar.

Under atmospheric conditions considerably different than what is assumed, T_{diff} varies by <1 K with a resulting difference in θ-bar of 0.7°. The uncertainty in T_{diff} scales roughly with T_{diff} itself and will be larger under circumstances with a higher angle of solar incidence or higher values of θ-bar. Incorrect atmospheric assumptions will have a greater effect on θ-bar determinations for greater values of θ-bar itself. As a result, under high values of θ-bar (10–15°) determined during periods of high atmospheric dust opacity and warm temperatures are likely underestimated by up to ∼1° (∼10% relative error).

3.2. Surface footprint size

The greatest source of uncertainty in θ-bar determination is due to the footprint of the TES EPF observation (Fig. 5). The two complimentary ∼20 by 80 km 65° emission angle observations are separated by ∼120 km at the equator and ∼60 km at 60° N/S latitude. For a reasonable determination of surface slope characteristics, these surfaces are required to be statistically identical. Slight changes in albedo, thermal inertia, and the surface roughness properties between the two measurements will have large effects on the derived θ-bar.

The magnitude of this effect is apparent from the data itself shown in the results section below. EPF observations taken under limited atmospheric, surface temperature, and solar incidence conditions within a small region display variations in θ-bar that exceed what would be expected from the uncertainties discussed above. For example, 39 EPF observations were collected within 180–230° E and 58–65° N, with solar incidence angles of 45–55° and surface temperatures between 230 and 265 K. Despite the uniformity of the terrain type, these observations have θ-bar values of 2.8° to 10.4° with a standard deviation of 1.3° and an average of 8.4°. While there could well be some natural variation in surface roughness characteristics, this range of θ-bar values is nearly as great as any systematic planet wide trends. If this variation is entirely due to inhomogeneities in the surface between the two EPF observations, the standard deviation of 1.3° results in a relative error of 15%.

TES EPF observations from OCK's 16277 and 18942 illustrate one possible cause of this variability. The two EPF sets have θ-bar values of 5.9° and 10.4° for OCK's 16277 and 18942, respectively. The two observations are offset so that the up-track measurement from OCK 18942 overlaps with the down-track measurement from OCK 16277 (Fig. 5). The surface albedo (which affects surface temperatures) is slightly lower where the two EPF sets overlap and slightly higher in both instances where they do not overlap. This results in a reduced T_{diff} for the OCK 16277 observations and an increased T_{diff} for the OCK 18942 observations, consistent with the derived θ-bar values.

With enough individual EPF observations within a region, this variation will average out because the scatter in derived θ-bar values is essentially random. However, the large amount of potential scatter for any individual observation makes the interpretation of single TES EPF sets difficult. Bandfield and Smith (2003) used similar TES EPF observations to derive surface and atmospheric spectral properties and also found averages more reliable than individual observations. As will be shown in Section 4, regional variations are clearly apparent in the data and are not obscured by this source of noise.

There was an ∼8 min duration between the acquisition of the two complimentary observations. However, because planetary rotation was not accounted for, the local time at the measurement surface did not change. As a result, it is unnecessary to account for the slight cooling of the surfaces that would be expected over 8 min at the local time of the TES measurements.

3.3. Model uncertainties

A number of uncertainties are present in the inputs to the thermal model as well as inherent in the model itself. In order to gain insight into the sensitivity of the derivation of θ-bar to these uncertainties, we chose to investigate the effects of varying three parameters; albedo, thermal inertia, and atmospheric dust opacity. While there are a number of other parameters that are used in the thermal model (e.g. dust single scattering albedo, surface emissivity, etc.), the three parameters chosen here have similar effects as other parameters, namely uncertainties in the total energy reaching the surface, scattered versus direct downwelling radiance, and thermal diffusion into the subsurface.

We chose the surface conditions and geometry of TES EPF OCK 9938 as a typical set of conditions under which to test these sensitivities. This observation has a latitude of 67° N, L_s of 99, local time of 1385, surface cover thermal inertia of 250 J m^{-2} K^{-1} s$^{-1/2}$, albedo of 0.21, 9 μm dust opacity of 0.15, solar incidence of 46°, and observation emission angles of 66° and 67° from 172° and 352° azimuth from north, respectively. T_{diff} versus θ-bar was calculated using these conditions as a baseline. We varied albedo by ±0.02 and ±0.05, inertia by ±50 and ±100 J m^{-2} K^{-1} s$^{-1/2}$, and visible wavelength opacity by ±0.05 and ±0.10 (Fig. 4; Table 2). Uncertainties generally become greater for larger values of T_{diff} (and consequently the derived θ-bar) and are reported here for θ-bar values of 8 and 12. These are moderate and large values respectively that are observed in the data.

Relatively large changes in albedo have little effect on T_{diff} and the derived θ-bar. An error of ±0.05 in albedo causes a change the derived θ-bar by +0.26° and −0.21° at an original θ-bar of 12° and by ±0.13 at an original θ-bar of 8°. The effects of uncertainties in thermal inertia and opacity are somewhat larger. An error of ±0.10 in the visible dust opacity causes a change of +0.59° and −0.34° at an original θ-bar of 12° and by +0.28° and −0.23° at an original θ-bar of 8°. An error of ±100 J m^{-2} K^{-1} s$^{-1/2}$ in the thermal inertia causes a change of +0.47° and −0.29° at an original θ-bar of 12° and by +0.22° and −0.20° at an original θ-bar of 8°.

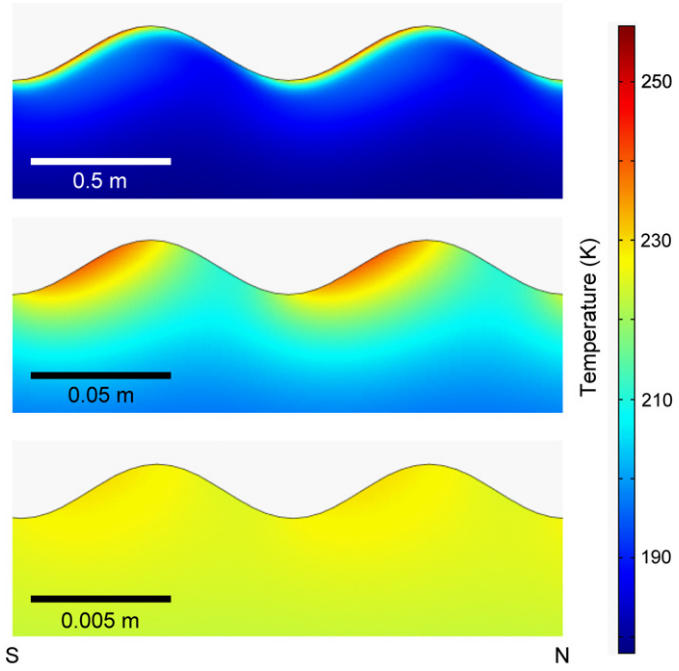

Fig. 3. Temperature cross sections at 1400 H of surfaces with a thermal inertia of 250 J m^{-2} K^{-1} s$^{-1/2}$. The surface features are essentially east–west trending linear grooves which maximizes the solar energy input to sunlit versus shaded surfaces. The wavelength of the features varies from 1 m (top) to 0.01 m (bottom). Surface temperature differences between the sunlit and shaded surfaces with the greatest slopes are listed in Table 1.

Table 1
Maximum temperature differences predicted for the 2-D surface model shown in Fig. 3 and described in the text

Inertia/scale	0.01 m	0.1 m	1 m	∞ (1-D model)
50	25 K	38	38	36
250	3.0	20	36	34
800	0.3	2.8	17	27

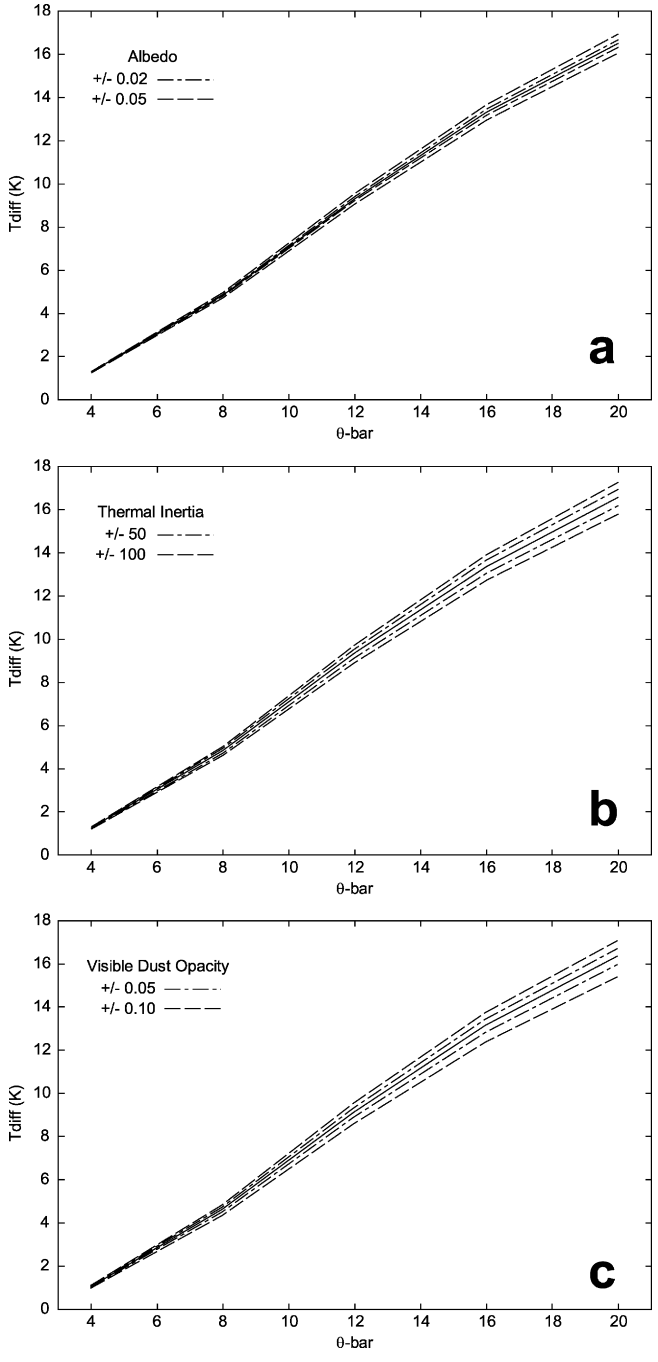

Fig. 4. Effects of albedo (a), thermal inertia (b), and visible dust opacity (c) on T_{diff} versus θ-bar. These effects are discussed in the text and listed in Table 2.

This sensitivity analysis indicates that even with relatively large uncertainties in parameters such as albedo, thermal inertia, and dust opacity, the resulting error in the derived θ-bar is significantly less than 1° (<5% relative error; Table 2) even at large values of T_{diff} and θ-bar. As discussed in Section 3.2, these uncertainties are small relative to the variations observed in the data due to the large footprint size of each TES EPF observation.

In addition, the model assumes a random distribution of slopes and slope azimuths. There are a number of common geologic features that can display a distinct non-random distribution of slope azimuths, such as duneforms and yardangs. These features, in extreme cases, can result in a wide range of derived θ-bar values. Care must be taken to identify the potential effects of these types of surfaces.

3.4. Feature size sensitivities (2-D model results)

Thermal diffusion through a material will diminish the temperature difference between sunlit and shaded slopes of smaller surface features. For example, there will be a much greater temperature difference between the sunlit and shaded sides of a large boulder versus a small pebble (Jakosky et al., 1990). It is critical to understand the scales at which the measurements are sensitive to gain an understanding of the surface properties.

We used a 2-dimensional thermal model with martian atmospheric and orbital parameters identical to the 1-dimensional KRC model described above to gain insight into the sensitivity of the scale of surface features on temperature. The modeled surface is a simplistic set of sine waves with the total amplitude set to 0.2 times the wavelength (Fig. 3). The wavelength scales were set to 0.01, 0.1, and 1 m each for surface thermal inertia

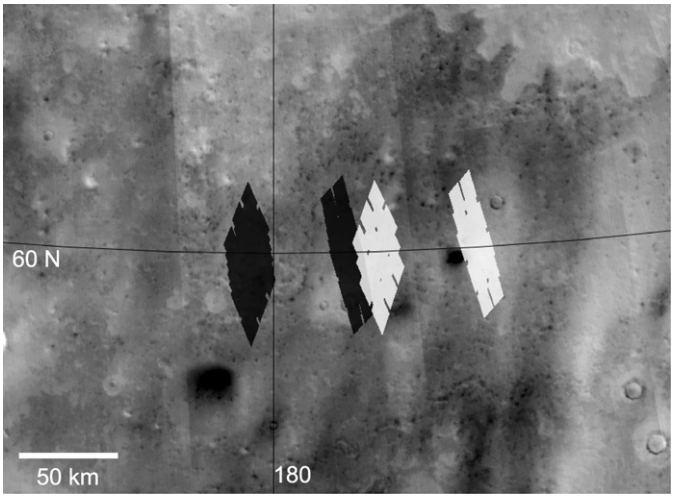

Fig. 5. TES footprints from EPF observations from OCK 16277 (black) and OCK 18942 (white). Within each observation, the right ground track is observed at a ∼65° emission angle from the south and the left ground track is observed at a ∼65° emission angle from the north. Each ground track consists of 18 separate bolometer measurements from 6 detectors collected during a 6 s time span. The albedo variations within the region contribute to variable surface temperatures that cause scatter in the derived surface slope characteristics.

values of 50, 250, and 800 J m^{-2} K^{-1} s$^{-1/2}$ (Table 1). The axis of the sine waves are aligned orthogonal to the solar azimuth at 1400 H (the local time of the TES observations) to maximize T_{diff} for this particular geometry. For this example, the density of the surface material was set to 1500 kg/m^3, the latitude was 67° N, elevation of −4300 m, and L_s of 100. Other seasons and locations will result in a variety of temperature differences, but the relative magnitude of the temperature difference with the scale of surface feature does not change dramatically.

As expected, the maximum temperature difference (note that this is not the same value as T_{diff}, which includes all surfaces within view of the observing spacecraft) between sunlit and shaded surfaces occurred for the largest surface features with the lower thermal inertia values (Table 1). Larger surface features have a greater physical separation between sunlit and shaded surfaces, which allows for larger temperature differences to be maintained (Fig. 3). High thermal inertia materials (with their associated higher thermal conductivity) do not maintain sunlit versus shaded surface temperature differences as well as insulating lower thermal inertia materials. Table 1 clearly shows that sensitivity to the scale of feature is dependent on the thermal inertia of the feature itself and surfaces with extremely high or low thermal inertia values will be sensitive to m and cm scale features, respectively. Moderate thermal inertia values (which are most common for the martian surface) appear to maintain significant temperature differences at scales of 0.1 m and larger. As will be discussed below, surface roughness is typically dominated by the smallest scale of sensitivity. The 0.1 m scale of sensitivity to thermal infrared measurements for typical martian conditions compliments the sensitivity of visible photometry measurements to <0.1 m scales (Helfenstein and Shepard, 1999) and the >3 m scales determined from photoclinometry and other methods (e.g. Kirk et al., 2003; Beyer et al., 2003).

A noteworthy aspect of the modeling simulation is the lack of large temperature differences that can be maintained by high inertia surfaces, such as rocks. The combination of higher conductivity and lower daytime temperatures (resulting in a lower difference in radiance for a given difference in temperature) prevents sub-meter scale rocks from contributing greatly to the apparent temperature differences measured in TES EPF observations. Directional field temperature measurements of Jakosky et al. (1990) produced similar results. In that study, large blocks (∼1 m) from an a'a flow displayed greater temperature disparities between sunlit and shaded surfaces than the sunlit and shaded surfaces of cobbles or pebbles. In addition, rocks are typically a relatively small percentage of the surface and surface thermophysical properties are largely dominated by the surface fines (Christensen, 1986).

3.5. Summary

The largest uncertainties in the derivation of surface roughness characteristics are largely due to the scatter present because of the large footprint size of the TES EPF observations. While other uncertainties can also influence the derivation of θ-bar, the focus of the technique on the differences in temperatures rather than the absolute measured temperatures minimizes the effects of these uncertainties. With more precise targeting, such as what MCS is capable of, this scatter can be reduced considerably. This would allow for a better evaluation of the true precision of this technique as well as a better assessment of the surface roughness characteristics of for more tightly focused regions.

4. Results

4.1. Global dataset

The 4545 derived θ-bar values were stored in a table with other information, such as surface temperatures and geometry, for each TES EPF sequence. We investigated the relationship of θ-bar versus latitude, longitude, and albedo to identify the trends present between these parameters and surface slopes.

The planet wide average θ-bar value is 6.7° with 57% of the values falling between 2° and 8° and 95% between 0° and 12°. Fig. 6 displays a global map of θ-bar values as well as the occurrence of θ-bar values with respect to latitude. There are distinct trends within latitude bands. High latitude regions >50° display relatively high θ-bar values. The 10–30° N latitude range has the lowest θ-bar values with 81% falling between 0° and 6°.

Most TES EPF observations were taken at 15° latitude intervals and it is possible to look at θ-bar values with respect to longitude at specific latitudes (Fig. 7). Several latitudes, such as at 30° N, do not show much systematic variation of θ-bar with longitude. Other regions, such as 15° S, display prominent variations with longitude. For example, 240–300° E and 0–40° E have low values of θ-bar relative to other longitudes within the 15° S latitude band. In addition, Hellas basin at 45° S also have low values of θ-bar relative to other surfaces at similar latitudes (Fig. 7).

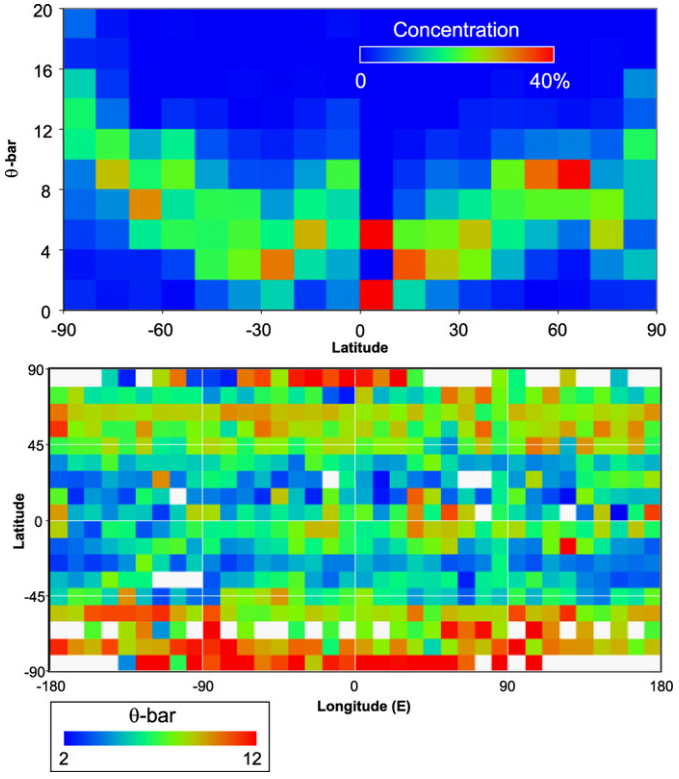

Fig. 6. Top: Concentration of θ-bar values in 2° bins versus latitude in 10° bins. Concentrations are normalized within each latitude band. Bottom: Global map of θ-bar values binned in 10° of latitude and longitude. White areas indicate where no data is present.

Extreme values of θ-bar (>14°) are common at high southern latitudes. There are several high θ-bar values at lower latitudes, several of which coincide with Valles Marineris and the region southwest of Arsia Mons. In the case of the Valles Marineris observations, there are clear indications that the observations coincided with the north facing slopes of the canyon walls, which enhanced the temperature disparities between the north and south facing azimuth observations, which only satisfied the solar incidence constraints during the northern summer season. A number of high θ-bar observations are also located in the far northern regions (>75° N) that appear to coincide with the polar sand seas and regions of residual summer ice. There are a number of other scattered high θ-bar observations that do not appear to show any spatial correlations or trends.

Unusually low θ-bar values (<2°) are somewhat more scattered than the higher values. The greatest concentration of low θ-bar values is located at southern hemisphere mid to high latitudes with a lesser concentration at northern hemisphere low to mid latitudes. Extremely low θ-bar values are not common at the equator (though these observations are limited in number by solar incidence constraints) or at latitudes north of 45° N.

A distinct θ-bar versus albedo trends is apparent as well (Fig. 8). Higher θ-bar values are associated with moderate albedo values (θ-bar >6° for 55% of the observations at albedos between 0.1 and 0.25) and lower values are associated with higher and lower albedo surfaces (θ-bar <6° for 67% of the observations at albedos >0.25 and 58% at albedos <0.1).

Table 2
Sensitivity of the derived θ-bar parameter to variations in surface albedo, opacity, and thermal inertia inputs to the thermal model and variations in atmospheric correction parameters for surface temperature determination

Parameter	θ-bar = 8°	θ-bar = 12°
Albedo		
±0.02	±0.06° (1%)	+0.12/–0.10 (1)
±0.05	±0.13 (2)	+0.26/–0.21 (2)
Opacity		
±0.05	+0.12/–0.10 (1–2)	+0.20/–0.14 (1–2)
±0.10	+0.28/–0.23 (3–4)	+0.59/–0.34 (3–5)
Thermal inertia		
±50	±0.10 (1)	+0.22/–0.14 (1–2)
±100	+0.22/–0.20 (3)	+0.47/–0.29 (2–4)
Atmospheric correction		
None	−0.6 (8)	
T_{atm} + 20 K and 3× opacity	+0.7 (9)	

4.2. Local regions

A number of regions were investigated in detail because they have been well characterized as landing sites or because they displayed unusually high or low θ-bar values (Table 3). The north polar sand seas, high southern latitudes and a region southwest of Arsia Mons have high θ-bar values >11. Conversely, the Tharsis region and the Southern Highlands (at 30° S, 25° E) was chosen as representative of a number of regions that have low θ-bar values (<3°). For each of these sites, corresponding high resolution (⩽6 m/pixel) MOC images within each region were analyzed.

A number of EPF observations were acquired over the Viking 2 and MER-A landing sites with the temperature and solar incidence constraints described above. Though EPF's were specifically targeted for the MER landing sites for coordinated atmospheric observations (Wolff et al., 2006), none were acquired for either the Viking 1 or Pathfinder landing sites. Observations were also acquired within the proposed Phoenix Lander latitude range (65–72° N). Observations were not specifically targeted for the Viking 2 landing site and, as a result, the EPF listed in Table 3 is ∼150 km away from the landing site, although the nature of the terrain appears similar. All landing sites have relatively high θ-bar values between 7.5° and 9.3° (Table 3).

5. Discussion

5.1. Average θ-bar and derived slope distributions

We chose to report the surface slope characteristics in terms of θ-bar because of its relative simplicity and its established use by previous photometry studies. However, θ-bar is not particularly intuitive or useful as a direct means of obtaining information regarding a surface. Generally, the greatest slopes occur at the smallest scales. As a result, θ-bar commonly represents the slope distribution at the smallest scales that the measurements are sensitive to (Shepard and Campbell, 1998; Helfenstein and Shepard, 1999; Cord et al., 2003). For exam-

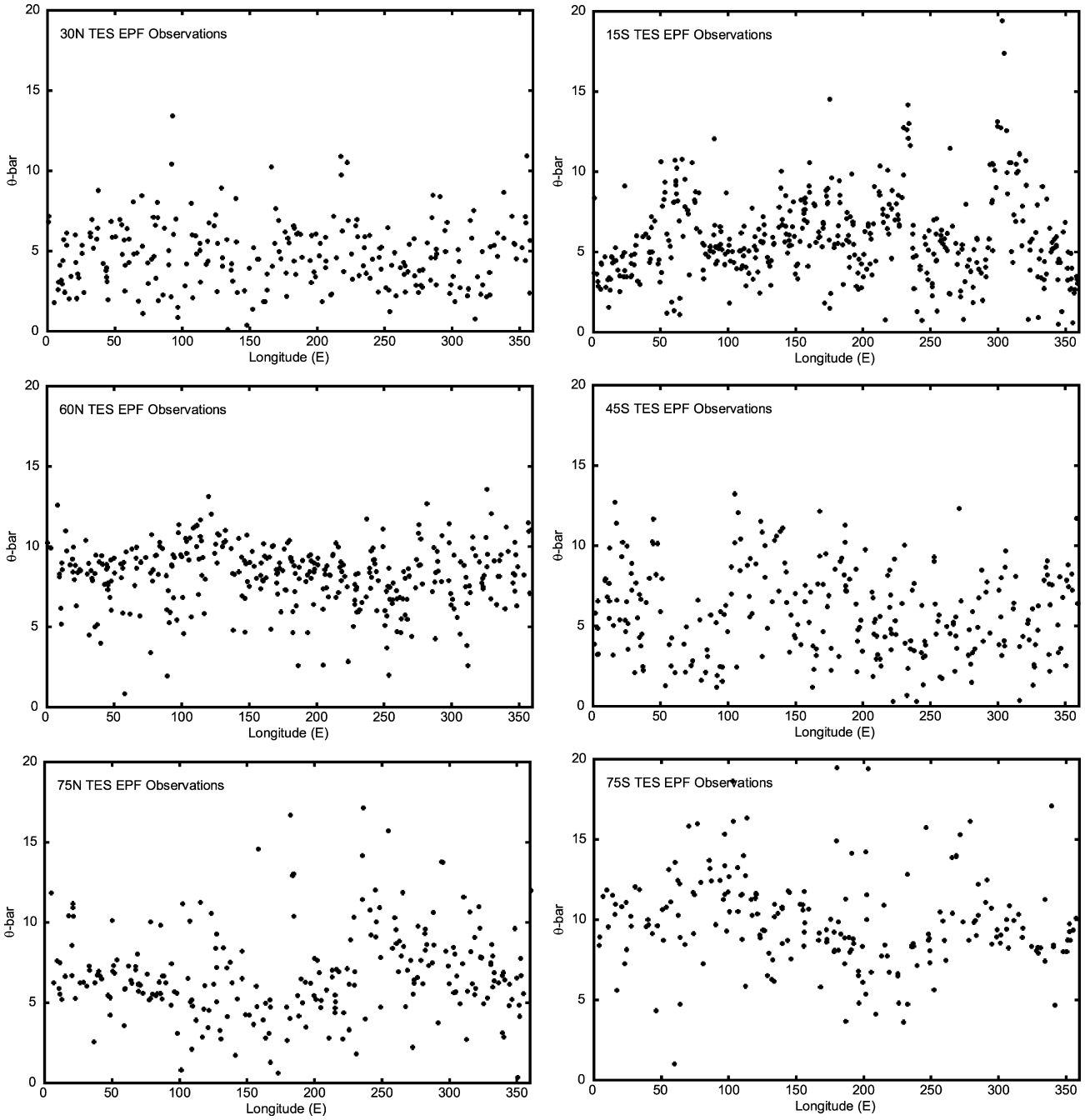

Fig. 7. θ-bar versus longitude at several latitudes. Each dot represents an individual TES EPF observation.

ple, Helfenstein and Shepard (1999) used Apollo Lunar Surface Closeup Camera images to determine this scale as ∼0.1 mm with almost no contribution from scales larger than 8 cm.

As discussed above, the thermal infrared measurements are sensitive to the size at which shaded slopes remain thermally isolated from sunlit slopes. This scale depends on the thermal inertia of the surface cover, with most martian surfaces having moderate inertias of 150–350 (Mellon et al., 2000; Putzig et al., 2005). The 2-dimensional modeling indicates that features with this thermal inertia range that are larger than ∼0.1 m will retain significant temperature differences between sunlit and shaded slopes. Thus, the θ-bar values derived from the TES EPF data are dominated by the distribution of slopes at ∼0.1 m scales for most of the martian surface.

There are several exceptions to this interpreted scale. (1) The Tharsis, Elysium, and Arabia regions of Mars have low thermal inertia surfaces ($<$100) that would indicate a sensitivity to slopes at scales of ∼0.01 m. (2) Dune fields are an example where surface roughness does not necessarily scale inversely with size and the derived θ-bar value will represent the scale of the dunes. This scaling behavior is exceptional and it is not clear if there may be other types of surfaces that follow this pattern. (3) Rocks have high thermal inertia values ($>$800) and can only maintain significant temperature differences between

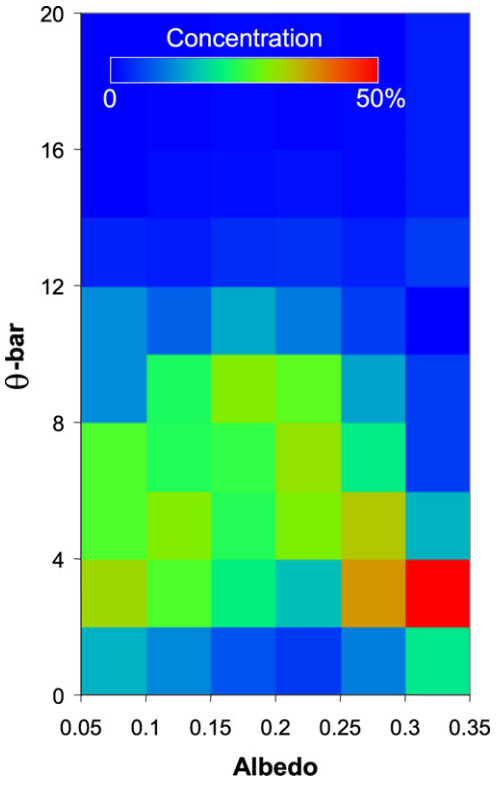

Fig. 8. Concentration of θ-bar values in 2° bins versus latitude in bins of 0.05. Concentrations are normalized within each albedo bin.

Table 3
Orbit numbers and locations of TES EPF observations for regions of interest discussed in the text

Description	OCK[a]	Latitude	Longitude	θ-bar
North polar sand dunes	10697	82	186	11.6°
Southwest of Arsia Mons	26142	−15	234	12.9
South pole	13858	−86	142	14.8
Southern high latitudes	6062	−75	97	15.4
Northern high latitudes	28207	75	92	4.6
Tharsis	12769	15	240	2.7
Southern highlands	17364	−30	25	1.2
MER-A	24963	−15	175	9.1
Phoenix 1	10608	67	231	7.5
Phoenix 2	8483	67	245	9.3
Viking lander 2	7066	45	135	8.5

[a] Orbit counter Keeper (MGS orbit number starting with Mars orbit insertion).

sunlit and shaded slopes at scales larger than ∼1 m. Because the majority of rocks on most martian surfaces are significantly <1 m in size (e.g. Golombek et al., 1999, 2003b) and for other reasons discussed in the sensitivities section (e.g. generally low radiance contribution to the measurement), the effect of rocks on the derivation of θ-bar is greatly diminished.

Slope characteristics at scales different than the scale of greatest sensitivity can be predicted based on the assumption of fractal behavior. This can be simply described by

$$s_x = s_{x_0}(x/x_0)^{H-1} \quad (1)$$

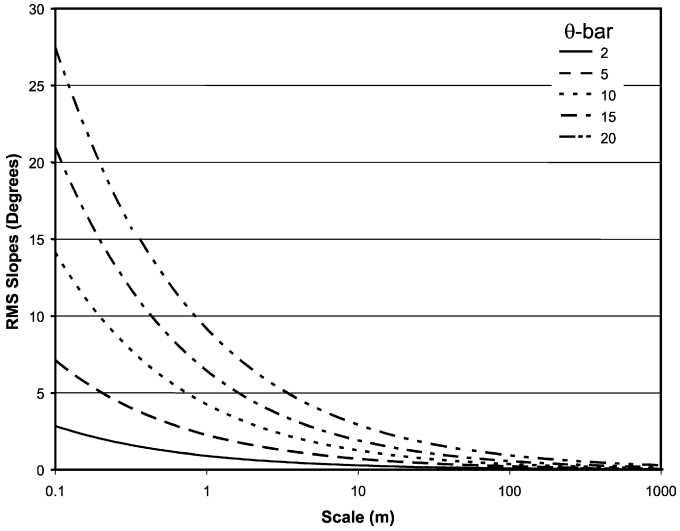

Fig. 9. Relationship between θ-bar and RMS slope angles at various scales using the relations in Eqs. (1) and (2). In this example, the smallest scale of sensitivity is 0.1 m and the Hurst exponent is 0.5.

In this equation, s is the RMS slope of a surface [$\tan(\theta_{\mathrm{RMS}})$] at the scale of interest, x, and a reference scale, x_0, and H is the Hurst exponent that describes how the RMS slopes scale with x. For example, at a value of $H = 1$, the RMS slopes will be equal at all scales. A value of $H = 0$ will result in RMS slopes that are highly dependent on the scale of interest. Most natural surfaces have a value of H near 0.5 (typical for scales of less than a few decimeters; Shepard et al., 2001).

There are limitations to the range of scales over which Eq. (1) can be applied. Surfaces often have "breakpoints" where the value of H changes at a certain length scale (Shepard et al., 2001; Campbell et al., 2003). This commonly occurs at a scale where the process affecting the surface morphology changes. For example, a lava flow has certain slope characteristics at <10 m scales, but, at larger scales, the slope characteristics are more indicative of the underlying topography (Shepard et al., 2001; Campbell et al., 2003). Larger scale surfaces almost always have a smaller value of H and the scale of this breakpoint usually occurs at scales of several centimeters to several meters.

Shepard and Campbell (1998) and Helfenstein and Shepard (1999) examine the relationship between θ-bar, scale, and fractal behavior. The following approximation can be applied:

$$\tan(\theta\text{-bar}) \approx 0.7 s_{x_0} \quad (2)$$

(Shepard and Campbell, 1998). In this case, s_{x0} is the smallest scale that the measurement is sensitive to, which is commonly ∼0.1 m for thermal infrared observations. For example, a surface with a θ-bar of 8.0° will have an RMS slope of 11.4° at 0.1 m scales. At 1 m scales the RMS slope is 3.6° (corresponding roughly to a θ-bar value of 2.5°). As a rule of thumb, with a value of $H = 0.5$, both θ-bar and RMS slopes scale by a factor of ∼1/3 ($10^{-0.5}$) with each order of magnitude in scale (Fig. 9). Although this relationship between θ-bar and RMS slopes assumes a value of $H = 0.5$, Helfenstein and Shepard (1999) have found this approximation remains good at other values of H.

There are a variety of possible values of H, but most surfaces have values that fall between 0.3 and 0.7 at meter and smaller scales. These values are generally smaller (0–0.3) for larger scales, which indicate that by assuming a value of $H = 0.5$, we will overestimate the slopes at larger scales (>10–100 m). These larger scales are easily imaged and have been well characterized with MOLA data as well (Kirk et al., 2003; Beyer et al., 2003; Anderson et al., 2003), making this extrapolation with the thermal infrared data not particularly useful anyhow. Hurst exponent values have been determined from MOC ($H = 0.7$) and MOLA ($H = 0.4$) data for length scales of >10 and >300 m, respectively (Kirk et al., 2003; Anderson et al., 2003). There is some disagreement in these numbers despite some overlap in the scale of measurements. However, these values fall within the range determined by other studies of natural surfaces. Slope characteristics at these larger scales may be poorly correlated with smaller scales, making any extrapolation between the two scales difficult (Campbell et al., 2003).

5.2. Comparison with photometric and terrestrial studies

Most lava flows and cobble dominated surfaces (e.g. active alluvial fans) are much rougher than indicated by the range of θ-bar values derived from the TES EPF data. However, mantled, dune, and playa surfaces have surface slope distributions at 0.1 m scales that fall within the range of martian values (Shepard et al., 2001). This is likely indicative of smaller particle sizes being the dominant surface cover, consistent with typical thermal inertia values for the martian surface (e.g. Kieffer et al., 1977; Mellon et al., 2000). It may also be partially due to the lack of influence of rocks on the derivation of θ-bar from thermal infrared measurements.

McEwen (1991) and Cord et al. (2003) reviewed the photometric parameters derived for Solar System bodies from visible imaging datasets. Most values of θ-bar from these studies fall between 10° and 30°, which is considerably higher than the average of 6.7° from the TES EPF observations. However, when considering the scale of sensitivity of the visible versus thermal measurements, there is qualitative agreement as the finer scales are expected to have greater values of θ-bar.

There are few orbital photometric studies of the martian surface largely because of the difficulty in accounting for atmospheric aerosol effects. A number of studies have investigated the photometric roughness of surfaces within the Viking, Pathfinder, and Mars Exploration Rover landing sites (Arvidson et al., 1989; Guinness et al., 1997; Johnson et al., 1999, 2006a, 2006b). These studies have shown the martian soils and dusty surfaces have θ-bar values between 4° and 27°. Initial photometric results from the Mars Express High Resolution Stereo Camera (HRSC) data indicate a range of derived θ-bar values similar to those derived from lander measurements (Jehl et al., 2006).

With such a large range of derived θ-bar values found within isolated locations, it is difficult to make a reasonable comparison with the orbital data. However, even when assuming a θ-bar of 27° for the visible wavelength measurements, high values of H (0.79) are required for the sub-millimeter visible measurements to scale well to the decimeter scale using Eq. (1).

While high values of H may be an intrinsic property of the martian surface, it may be more likely that there is a breakpoint present in the three orders of magnitude difference in the scale of sensitivity between the two measurement techniques. This is consistent with other reported values of surface roughness at centimeter to decameter scales (Shepard et al., 2001). It appears that surface roughness characteristics at sub-centimeter, sub-meter, and sub-kilometer scales are largely independent of one another. This is consistent with different processes shaping surface morphology at these three scales.

5.3. Comparison with photoclinometric studies

Photoclinometry (e.g. McEwen, 1991; Kirk et al., 2003; Beyer et al., 2003), has been used to assess surface slopes at scales as low as 3 m from MOC imagery. This allows for comparison to the slope results presented here from larger scales rather than the smaller scales of photometry discussed in Section 5.2. Kirk et al. (2003) and Beyer et al. (2003) both derived ⩾3 m slope statistics for candidate MER landing sites. 3–6 m baseline RMS slopes were highly variable even within landing site regions and corresponded with distinct surface units. For example Kirk et al. (2003) found RMS slopes of 0.9° to 16° for all sites and 4° to 16° within the Gusev Landing site region. The large range of RMS slope values derived from photometry was chosen to represent the range of surface types within the Gusev region. The cratered plains, which dominate the corresponding TES EPF measurements, have RMS slope values of ∼4–4.5°. A Hurst exponent of ∼0.65 is necessary for the 3 m scale measurements to scale in agreement with the IR measurements (θ-bar of 9.3°; listed in Table 3). As discussed in Section 5.6, these results are in good agreement with actual rover traverse statistics.

Despite the agreement in this one instance, a comparison of the range of values from both methods may indicate a disparity. The TES EPF measurements indicate that most values of θ-bar between 0 and 12 (about 0° to 17° RMS). This is almost exactly the same range as listed by Kirk et al. (2003), despite the fact that there is a factor of ∼30–60 difference in the scales of the two measurements. It may be that the range of sites investigated by Kirk et al. (2003) may not be suitable for comparison to the global sites, especially as rough terrains may be disproportionately represented. Many plains units, which presumably dominate martian surfaces, have lower values (1–4° RMS slopes) that are more consistent with the range of values presented here.

The large spatial scale of the TES measurements and the limited application of the photoclinometry prevent a more complete comparison. A detailed comparison of results from the two techniques, especially with higher spatial resolution infrared measurements, could potentially determine whether 0.1 and 3–10 m length scale slopes are correlated.

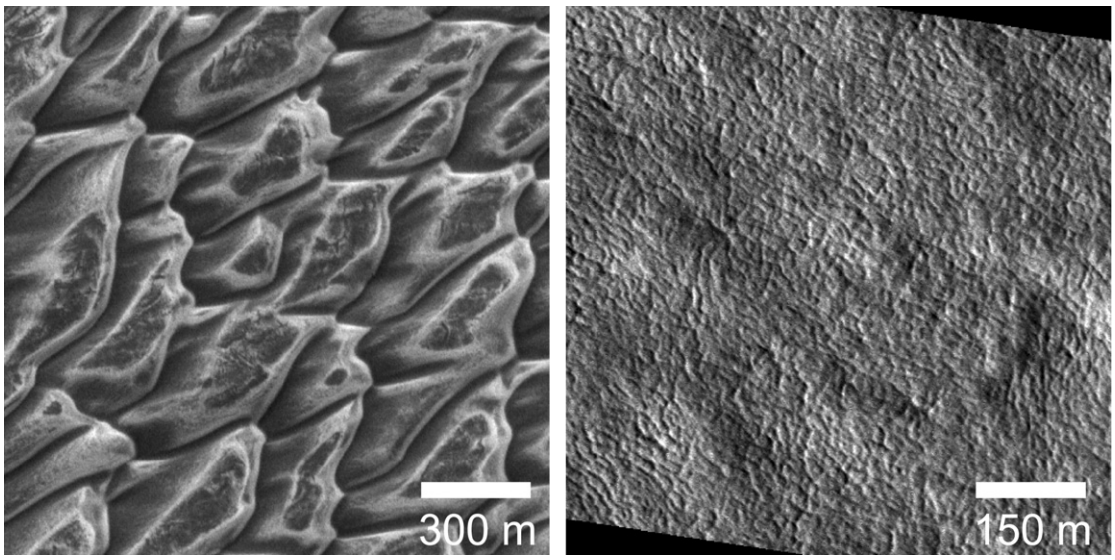

Fig. 10. MOC images E1500671 (left) and E1301252 (right) centered at 82.0° N, 181.7° E and 87.0° S, 111.9° E, respectively. These images are near TES EPF observations of the north polar sand dunes and south pole and are listed in Table 3.

5.4. Global trends

There are systematic global correlations of the derived surface slope characteristics with albedo, latitude, and longitude (Figs. 6–8). High albedo surfaces are generally indicative of dust cover that may form smooth surfaces that would explain their low θ-bar values. Classic martian high albedo regions such as Arabia Terra, Elysium, and Tharsis are all located at northern low to mid-latitudes. It is likely that part of the trend of θ-bar with latitude is due to the correlation of albedo with latitude. There is also a concentration of low θ-bar values near 30° S. This is associated with southern highlands low albedo surfaces. It is not clear what process would form these smooth surfaces. Low θ-bar values at restricted longitudes and 15° S or 45° S coincide with Tharsis and Hellas basin, which are high albedo, dusty regions (Fig. 7).

Higher θ-bar values are associated with high latitudes where the highest average θ-bar values are found between 50–70° N and south of 50° S. The greatest concentration of extremely high θ-bar values are found south of ∼60° S. These surfaces are dominated by periglacial surface properties apparent in high resolution images (e.g. Mangold, 2005). These types of surfaces typically have distinct features that are likely to have elevated slope distributions.

5.5. Comparison with local surface morphologies

The comparison of the derived θ-bar values with orbital imagery shows that 10 m scale surface morphology is a poor indicator of sub-meter scale morphology. We chose a number of exceptionally high and low θ-bar locations with coincident MOC imagery to illustrate this lack of correlation. This section provides a set of examples that shows both how disparate surface morphologies can have similar θ-bar values and how similar surface morphologies can have disparate θ-bar values.

Several regions show systematically high θ-bar values, including several high latitude regions and an area southwest of Arsia Mons. The pervasive sand dunes at high northern latitudes are clearly surfaces with high slope angles, and this is an example where the scale of the imaging is likely to be sensitive to the same features as the directional thermal infrared measurements (Fig. 10). Although ripples and other small scale features may form on dune surfaces, the 10s to 100s of meters scale of the dunes is the dominant scale of surface slopes.

Other regions are not clearly distinguished as unusually rough in orbital images. A region southwest of Arsia Mons (15° S, 230–235° E) displays anomalously high θ-bar values between 9.7° and 14.1°. Yardang features are pervasive throughout the region that would appear to explain the high θ-bar values (Fig. 11). However, a similar morphology is present in surfaces to the west that have θ-bar values of $<7°$. There also does not appear to be any albedo or thermal inertia correlations with this region. This discrepancy may be explained by the fact that processes that shape the surface at 10 m and larger scales can be independent of those operating at sub-meter scales. The surfaces in the region are likely to be friable volcanic ash or indurated dust deposits that may be quite rough at sub-meter scales. A possible explanation for the difference may be that where θ-bar values are relatively low, there may be a thin regolith cover, which would not necessarily affect the morphology or albedo in the orbital imagery.

High southern latitudes (south of ∼75° S) have the consistently highest θ-bar values on the planet (commonly $>8°$ and often $>12°$). These regions have a variety of surface morphologies, but most surfaces display significant surface textures at the finest scales discernible (Fig. 12). Patterned ground features appear to be present at a number of scales at these latitudes and are perhaps pervasive at meter scales even where they are not present at larger scales. This may be a cause of the high slopes present. However, corresponding northern high latitude surfaces can display similar morphologies at the highest scales,

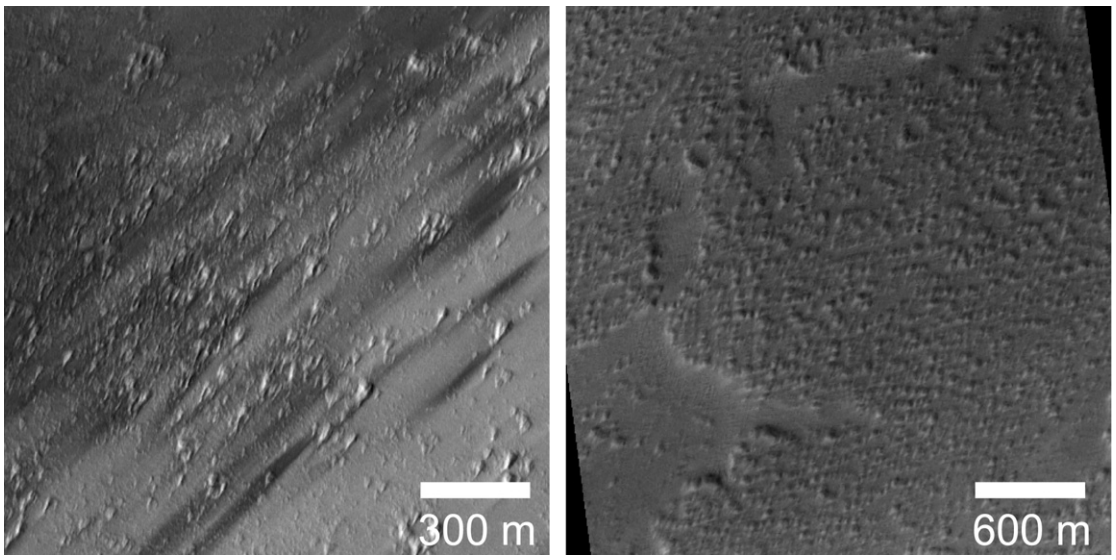

Fig. 11. MOC images M0905298 (left) and E1100650 (right) centered at 15.0° S, 226.7° E and 13.9° S, 233.8° E, respectively. The left image is in a region of moderate θ-bar values and the right image is in a region of high θ-bar values. Both images are southwest of Arsia Mons.

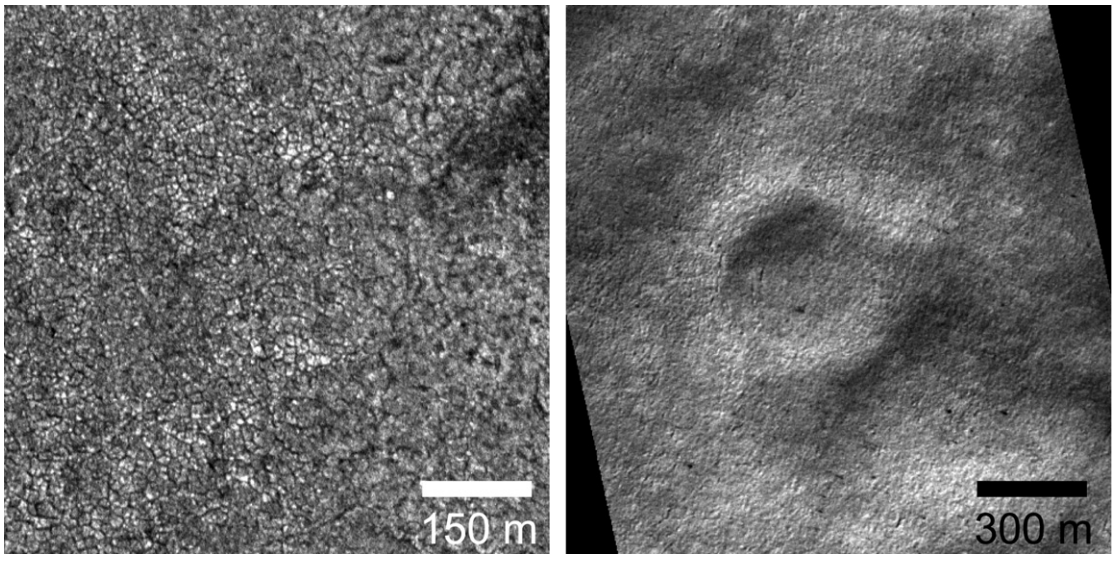

Fig. 12. MOC images M0202660 (left) and M0401825 (right) centered at 75.8° N, 91.4° E and 74.6° S, 98.2° E, respectively. These images are near TES EPF observations listed as northern and southern high latitudes in Table 3. The left image is in a region of low θ-bar values and the right image is in a region of high θ-bar values.

but have lower than average θ-bar values (Fig. 12, Table 3). One possible cause of this discrepancy is the presence of a nearby supply of eolian sand in the north which could get trapped in local depressions and smooth rough terrain. There is some indication that local depressions in some northern patterned ground regions are at least partially filled with lower albedo material.

Unusually smooth surfaces are apparent near 30° S and 0–30° N with θ-bar values commonly $<8°$ and often $<5°$. These two latitude regions have very different large scale morphologies. The southern region is dominated by low albedo highly cratered terrain and the northern region dominated by high albedo relatively lightly cratered surfaces. High resolution MOC images indicate that the southern latitude surfaces are smooth at high resolution (Fig. 13). These surfaces may be covered by a pervasive regolith, which would subdue meter and smaller scale topography but not necessarily have a large effect on larger scale surfaces. It is not clear what process would cause this region to be affected differently than other regions, however. Conversely, high albedo, low thermal inertia regions such as Tharsis, Arabia Terra, and Elysium at 0–30° N have much rougher appearing surfaces at 10–100 m scales (Fig. 13). These regions are thought to have significant dust deposits, which are likely to subdue surface roughness at sub-meter scales without affecting larger scale topographic features. For example, lava flow morphologies are clearly apparent throughout the Tharsis region even though thermal inertia values indicate that dust cover must be pervasive throughout the region.

The low thermal inertia values in high albedo regions such as Tharsis, Arabia Terra, and Elysium (<100, e.g. Kieffer et al., 1977) also indicates that the scale of sensitivity to the thermal

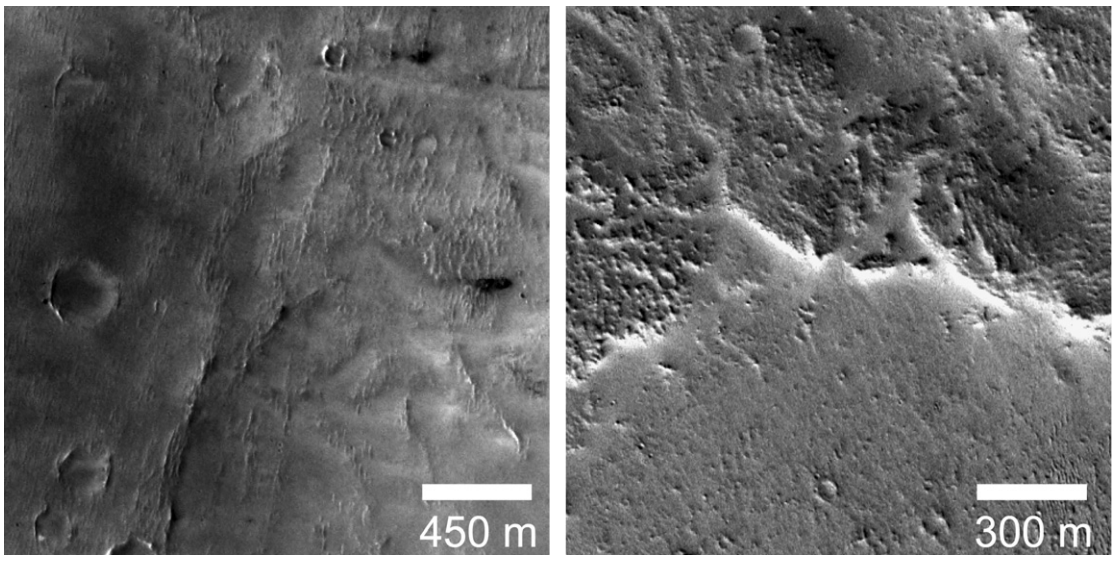

Fig. 13. MOC images R1103283 (left) and E1003798 (right) centered at 30.5° S, 24.0° E and 14.3° N, 239.5° E, respectively. These images both have low θ-bar values and are near TES EPF observations listed as Southern Highlands and Tharsis in Table 3.

infrared measurements is smaller than most other regions. The highly insulating surface prevents heat from effectively conducting to the shaded side of surface features as small as 1–2 cm (Table 1). In these regions, the measurements may be sensitive to scales an order of magnitude smaller than other regions with higher thermal inertia, such as the southern highlands example described above. These low thermal inertia, low θ-bar surfaces are likely to be extraordinarily smooth at centimeter to meter scales and are likely to be the smoothest regions on the planet. Assuming the scaling relationships discussed above, an average θ-bar of $\sim$3° for measurements sensitive to 0.01 m scales would scale to $\sim$1° at 0.1 m scales. At the 0.1 m scale, less than 5% of azimuth independent slopes are greater than 3°, assuming a Gaussian distribution of slopes. This is not surprising considering that the surfaces are likely to be dust mantled.

Radar observations indicate that many of these surfaces are unusually rough at centimeter to meter scales, however (e.g. Harmon et al., 1999). Radar observations can provide surface roughness properties at nearly the same scale as the thermal infrared measurements and should provide comparable results. Harmon et al. (1999) discuss how radar backscattering in these regions is consistent with extraordinarily rough lava flows but recognize that the low thermal inertia present in many of these regions precludes the exposure of these rough flows at the surface. In the case of a dust mantle, radar observations are likely to penetrate the surface with the shorter wavelengths preferentially attenuated (Harmon et al., 1999).

There is often little apparent correlation between θ-bar and surface morphology at greater than meter scales. Fig. 14 displays MOC images from a variety of surfaces that coincide with θ-bar values near 8°. These images display a number of different morphologies and apparent roughnesses at the 1.5–4.5 m/pixel scale. The Arsia Mons, and high southern and northern latitude examples described above display the opposite case of surfaces with variable θ-bar values, but similar surface morphologies in the images.

This disconnect may be explained by the processes that affect surface morphology at 10 m and larger versus sub-meter scales. In the first case, the landscape is often shaped by processes such as wind and water erosion and deposition, cratering, and mass wasting. Sub-meter scale morphologies are often dominated by the amount and nature of the regolith cover, which does not necessarily correspond to the landscape forming processes at larger scales. This result is similar to that of Shepard et al. (2001) and Campbell et al. (2003), which conclude that processes affecting surfaces at larger scales may operate largely independently of processes that affect surfaces at smaller scales.

5.6. Landing site characterization

Investigations of potential landing sites usually include restrictions on the slopes present at meter scales that would influence the stability of the spacecraft as well as potentially impact the energy collected by solar panels. Previous work done to characterize these slopes has focused on a combination of photoclinometry from high resolution images, Earth based radar, and laser altimeter measurements. Each of these techniques has been used to gain insight into the meter scale surface slope and roughness properties that have been validated by the lander missions (e.g. Golombek et al., 2003b). Use of thermal infrared measurements to obtain surface slope characteristics provides an additional independent measurement technique that has a unique set of sensitivities. It provides quantitative information about surface slopes close to the scale of interest that is highly complimentary to other surface characterization methods.

Table 3 shows that the 4 actual or potential landing site locations with TES EPF data have relatively similar θ-bar values between 7.5° and 9.3°. These are all moderately high values, but not close to that of some of the extreme values of θ-bar listed in Table 3, such as at southern high latitudes. As discussed above, these slope distributions are generally applicable

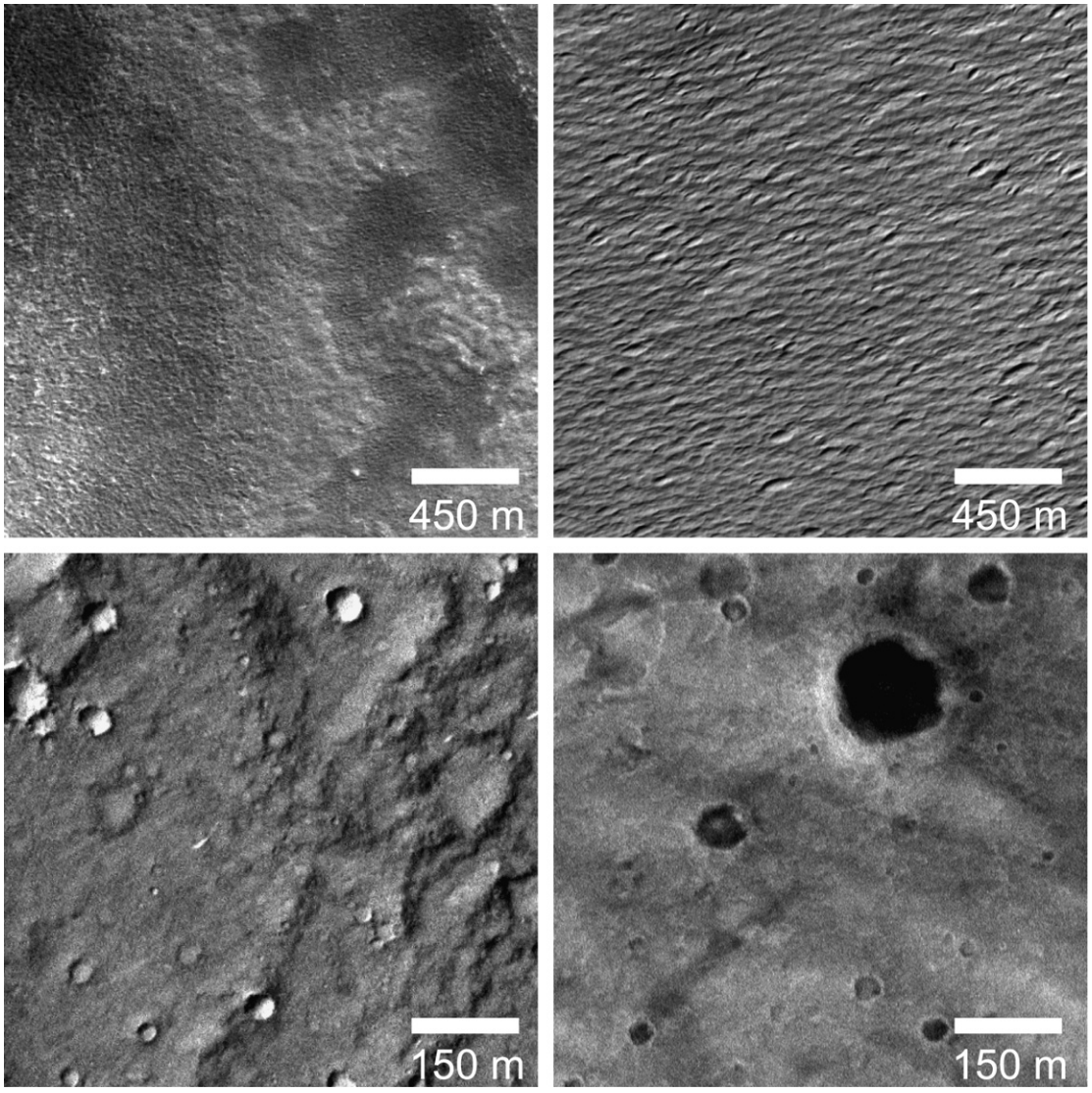

Fig. 14. MOC images E0200569 (upper left, 67.9° N, 230.9° E), M1801454 (upper right, 7.8° S, 199.5° E), R0300399 (lower left, 14.8° S, 174.9° E), and R0701606 (lower right, 14.7° S, 175.2° E). All images are near TES EPF observations that have θ-bar values of ∼8°.

to the smallest scale of sensitivity. Assuming that the fine component inertia at the various landing sites is generally moderate (Christensen, 1986), this scale is ∼0.1 m. This is smaller than what is necessary for characterization of lander safety, which is at ∼1 m scales. Using Eqs. (1) and (2), it is possible to predict slope distributions at these larger scales.

For example, a landing site requirement for the Phoenix Lander is that meter scale slopes cannot exceed 16°. Assuming a θ-bar of 9.3°, this translates into an RMS slope distribution of 13.3° at 0.1 m scales. Assuming a Hurst exponent of 0.7 (the high value was chosen to be conservative) and a scaling to 1 m, the RMS slope value is 4.7°. At this value, the probability of a 1 m scale slope exceeding 16° is less than 0.02. Using moderate values for θ-bar (8.5°) and the Hurst exponent (0.5), the 1 m scale RMS slope value is 3.8° and the probability of a 1 m scale slope exceeding 16° is less than 0.00001. Caution should be exercised when interpreting the low probabilities of high slope angles as Kirk et al. (2003) found high slope angles more common than would be predicted by Gaussian behavior. This has little effect on landing site characterization as the probabilities are still generally <1%.

Under these assumptions and conditions, θ-bar would need to exceed 10.8° or 17.0° to have more than 5% of 1 m scale slopes exceed the 16° limit, assuming a Hurst exponent of 0.7 and 0.5, respectively. Some caution should be used when interpreting these numbers and the scale of sensitivity should be noted, however. For example, as discussed above, θ-bar values derived from measurements over a dune field will not need scaling. Using the north polar dune field example listed in Table 3, the derived θ-bar is 11.6°, which is the equivalent of an RMS slope angle of 16.3°. As would be expected from this terrain, over 50% of the meter scale slopes exceed 16°, under these circumstances.

These slope distributions are not necessarily directly comparable to those obtained by other methods. This is primarily because of the lack of influence of sub-meter scale rocks on the value of T_{diff} and derived θ-bar (Fig. 15). For example, the difference in rock abundance between the Gusev crater and

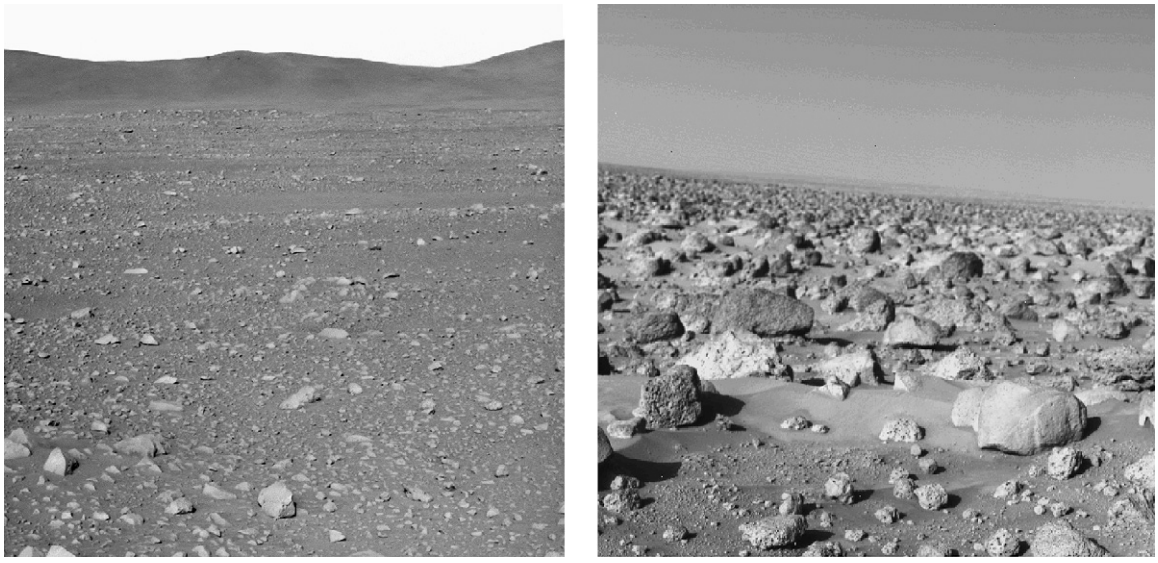

Fig. 15. MER-A (left) and Viking Lander 2 (right) images of Gusev crater and Utopia Planitia, respectively. The θ-bar values of these two sites are similar at 9.1° (MER) and 8.5° (VL2) despite the clear difference in surface roughness due to rocks at the two sites. Images are portions of PIA05875 and PIA00364 from http://photojournal.jpl.nasa.gov/. Images are courtesy of NASA, JPL, and Cornell University.

Utopia Planitia landing sites does not result in a pronounced difference in the derived θ-bar as the technique is sensitive to the underlying, relatively gentle slopes. In this manner, the technique presented here can compliment other surface characterization methods such as radar backscatter, thermal inertia and rock abundance measurements, and direct boulder counts from high resolution imagery. The directional thermal infrared measurements are more sensitive to the underlying topography rather than rocks that are protruding from the surface.

One potentially interesting comparison can be made between the rover traverse telemetry at Gusev with the results presented here. The rover traverse generally avoids rocks, allowing for a relatively direct comparison to the IR data (though still at larger length scales). Golombek et al. (2005) found RMS slopes at 3–10 m scales (for comparison with photoclinometry results) to be 2.5° with a Hurst exponent of 0.58. The 9.1° value of θ-bar listed in Table 3 translates to RMS slopes of 1.9° and 3.1° at 3 and 10 m respectively for this Hurst exponent. These measurements indicate a good agreement in an instance where ground truth is available. Given the differences in spatial sampling, the precise agreement between these results is likely somewhat fortuitous, however.

5.7. Future applications

Although the TES EPF observations have shown the ability to provide regional surface slope characteristics, their relatively large spot size and the inability to account for planetary rotation makes it difficult to focus on specific regions, such as potential landing sites. In addition the fixed 2AM/PM local time of the MGS orbit prevented the acquisition of equatorial surfaces under optimal conditions (a high solar incidence aligned with viewing azimuth).

Both the MCS and THEMIS instruments have the ability to collect multiple emission angle observations at higher spatial resolutions than TES. MCS has a footprint of $\sim 1/3$ the size of TES and 2-axis pointing capability that could compensate for planetary rotation. This would allow the targeting of ~3–5 km spots on the surface. Because the MCS measurements are similar in accuracy and precision to those of TES, it would be easy to adapt this technique to this dataset.

Use of this technique with THEMIS data would require more specialized targeting involving a pitch of the spacecraft. However, the high spatial resolution (~400 m/pixel at 65° emission angles) and precision (NEΔT $<$1 K at 245 K) of THEMIS data within an image would make it possible to obtain surface slope images of targeted regions. The spatial information associated with the surface slope characteristics would provide a significant improvement over the existing technique for the interpretation of the data.

6. Conclusions

Directional temperature measurements from TES EPF observation sequences display significant anisothermality consistent with the presence of surface slopes. These measurements are most sensitive to 0.1 m scales for surfaces with moderate thermal inertia. Lower thermal inertia surfaces are sensitive to scales as small as 0.01 m. Higher thermal inertia surfaces (consistent with rocks) conduct heat to shaded surfaces more efficiently and will not maintain significant temperature differences between sunlit and shaded surfaces at scales less than ~1 m.

A surface model of a Gaussian distribution of azimuth independent slopes (θ-bar) can be combined with a thermal model to predict surface temperatures and the apparent surface temperature from any emission angle and azimuth. This model can be used to predict the difference in apparent surface temperature for surfaces with different slopes from the different observation angles in the TES EPF sequences. The largest source of

uncertainty in the derivation of surface slopes from the TES observations is due to the inability to account for planetary rotation with the single axis pointing capability of TES. This requires large, statistically uniform regions, which are not always present.

Retrieved θ-bar values for most martian surfaces fall between 0° and 12° with an average of 6.7°. There are distinct correlations with albedo, latitude, and longitude within restricted latitudes. Regions with high slopes are concentrated at high latitudes. In the south, high slopes are associated with patterned ground of various types at latitudes greater than ∼60°. In the north, similar patterned terrains do not display high slopes, possibly because of eolian infilling of surface cracks with sand or other sediment. High slope angles in the north are associated with duneforms as would be expected.

The locations with the lowest slopes are located within the southern highlands at low latitudes and in high albedo, dusty regions. Several locations, such as within Tharsis and the Elysium volcanic regions display evidence for low slope angles from the thermal infrared observations coincident with regions of high radar backscatter returns. This is consistent with a significant mantling of dust that is penetrated by the microwave observations. There is little correlation between the apparent roughness at visible imaging scales and those detected at sub-meter scales by the infrared observations. This disconnect supports a similar conclusion of Campbell et al. (2003).

Surface slopes derived from directional thermal infrared observations can be used to characterize potential landing sites. This method is highly complimentary to other landing site characterization methods. Most locations generally have low surface slope angles at the meter scale, consistent with previous landing sites and other landing site characterization methods.

More precise targeting by current and future infrared observations such as those from MCS and THEMIS could significantly reduce uncertainties and surface spot size. This would allow for the surface slope characterization at sub-kilometer scales.

Acknowledgments

We would like to thank Sylvain Piqueux for providing the 2-D thermal modeling discussed in the text and shown in Fig. 3. Thanks also to Robin Fergason, who provided an early review of this manuscript. Jeff Moersch and Matt Golombek provided formal reviews that improved both the clarity and quality of this manuscript. Part of this work was funded by a grant from the Jet Propulsion Laboratory under the Critical Data Products (CDP III) Initiative for landing site characterization.

References

Anderson, F.S., Haldemann, A.F.C., Bridges, N.T., Golombek, M.P., Parker, T.J., Neumann, G., 2003. Analysis of MOLA data for the Mars Exploration Rover landing sites. J. Geophys. Res. 108, doi:10.1029/2003JE002125.

Arvidson, R.E., Guinness, E.A., Dale-Bannister, M.A., Adams, J., Smith, M., Christensen, P.R., Singer, R.B., 1989. Nature and distribution of surficial deposits in Chryse Planitia and vicinity, Mars. J. Geophys. Res. 94, 1573–1587.

Bandfield, J.L., Smith, M.D., 2003. Multiple emission angle surface–atmosphere separations of thermal emission spectrometer data. Icarus 161, 47–65.

Baron, J.E., Simpson, R.A., Tyler, G.L., Moore, H.J., Harmon, J.K., 1998. Estimation of Mars radar backscatter from measured surface rock populations. J. Geophys. Res. 106, 22695–22712.

Beckmann, P., 1965. Shadowing of random rough surfaces. IEEE Trans. Antennas Propag. 13, 384–388.

Beyer, R.A., McEwen, A.S., Kirk, R.L., 2003. Meter-scale slopes of candidate MER landing sites from point photoclinometry. J. Geophys. Res. 108, doi:10.1029/2003JE002120.

Campbell, B.A., 2001. Radar backscatter from Mars: Properties of rock-strewn surfaces. Icarus 150, 38–47.

Campbell, B.A., Ghent, R.R., Shepard, M.K., 2003. Limits on inference of Mars small-scale topography from MOLA data. Geophys. Res. Lett. 30, doi:10.1029/2002GL016550.

Christensen, P.R., 1986. The spatial distribution of rocks on Mars. Icarus 68, 217–238.

Christensen, P.R., and 25 colleagues, 2001. Mars Global Surveyor Thermal Emission Spectrometer experiment: Investigation description and surface science results. J. Geophys. Res. 106, 23823–23872.

Clancy, R.T., Wolff, M.J., Christensen, P.R., 2003. Mars aerosol studies with the MGS TES emission phase function observations: Optical depths, particle sizes, and ice cloud types versus latitude and solar longitude. J. Geophys. Res. 108, doi:10.1029/2003JE002058.

Cord, A.M., Pinet, P.C., Daydou, Y., Chevrel, S.D., 2003. Planetary regolith surface analogs: Optimized determination of Hapke parameters using multi-angular spectro-imaging laboratory data. Icarus 165, 414–427.

Fergason, R.L., Christensen, P.R., Kieffer, H.H., 2006. High-resolution thermal inertia derived from the Thermal Emission Imaging System (THEMIS): Thermal model and applications. J. Geophys. Res. 111, doi:10.1029/2006JE002735.

Garvin, J.B., Frawley, J.J., Abshire, J.B., 1999. Vertical roughness of Mars from the Mars Orbiter Laser Altimeter. Geophys. Res. Lett. 26, 381–384.

Golombek, M., Rapp, D., 1997. Size–frequency distributions of rocks on Mars and Earth analog sites: Implications for future landed missions. J. Geophys. Res. 102, 4117–4130.

Golombek, M.P., Moore, H.J., Haldemann, A.F.C., Parker, T.J., Schofield, J.T., 1999. Assessment of Mars Pathfinder landing site predictions. J. Geophys. Res. 104, 8585–8594.

Golombek, M.P., and 21 colleagues, 2003a. Selection of the Mars Exploration Rover landing sites. J. Geophys. Res. 108, doi:10.1029/2003JE002074.

Golombek, M.P., Haldemann, A.F.C., Forsberg-Taylor, N.K., DiMaggio, E.N., Schroeder, R.D., Jakosky, B.M., Mellon, M.T., Matijevic, J.R., 2003b. Rock size–frequency distributions on Mars and implications for Mars Exploration Rover landing safety and operations. J. Geophys. Res. 108, doi:10.1029/2002JE002035.

Golombek, M.P., Arvidson, R.E., Bell III, J.F., Christensen, P.R., Crisp, J.A., Crumpler, L.S., Ehlmann, B.L., Fergason, R.L., Grant, J.A., Greeley, R., Haldemann, A.F.C., Kass, D.M., Parker, T.J., Schofield, J.T., Squyres, S.W., Zurek, R.W., 2005. Assessment of Mars Exploration Rover landing site predictions. Nature 436, doi:10.1038/nature03600.

Guinness, E.A., Arvidson, R.E., Clark, I.H.D., Shepard, M.K., 1997. Optical scattering properties of terrestrial varnished basalts compared with rocks and soils at the Viking Lander sites. J. Geophys. Res. 102, 28687–28704.

Hagfors, T., 1964. Backscattering from an undulating surface with applications to radar returns from the Moon. J. Geophys. Res. 69, 3779–3784.

Hagfors, T., 1968. Relations between rough surfaces and their scattering properties as applied to radar astronomy. In: Evans, J., Hagfors, T. (Eds.), Radar Astronomy. McGraw–Hill, New York, pp. 187–218.

Hapke, B., 1981. Bidirectional reflectance spectroscopy. 1. Theory. J. Geophys. Res. 86, 4571–4586.

Hapke, B., 1984. Bidirectional reflectance spectroscopy. III. Correction for macroscopic roughness. Icarus 59, 41–59.

Harmon, J.K., Ostro, S.J., 1985. Mars—Dual-polarization radar observations with extended coverage. Icarus 62, 110–128.

Harmon, J.K., Arvidson, R.E., Guinness, E.A., Campbell, B.A., Slade, M.A., 1999. Mars mapping with delay–Doppler radar. J. Geophys. Res. 104, 14065–14090.

Helfenstein, P., 1988. The geological interpretation of photometric surface roughness. Icarus 73, 462–481.

Helfenstein, P., Shepard, M.K., 1999. Submillimeter-scale topography of the lunar regolith. Icarus 141, 107–131.

Jakosky, B.M., Finiol, G.W., Henderson, B.G., 1990. Directional variations in thermal emission from geologic surfaces. Geophys. Res. Lett. 17, 985–988.

Jämsä, S., Peltoniemi, J.I., Lumme, K., 1993. Thermal emission from a rough surface: Ray optics approach. Astron. Astrophys. 271, 319–325.

Jehl, A., and 16 colleagues, 2006. Improved surface photometric mapping across Gusev and Apollinaris from an HRSC/Mars Express integrated multi-orbit dataset: Implication on Hapke parameters determination. Lunar Planet. Sci. 37. Abstract 1219.

Johnson, P.E., Vogler, K.J., Gardner, J.P., 1993. The effect of surface roughness on lunar thermal emission spectra. J. Geophys. Res. 98, 20825–20830.

Johnson, J.R., and 18 colleagues, 1999. Preliminary results on photometric properties of materials at the Sagan Memorial Station, Mars. J. Geophys. Res. 104, 8809–8830.

Johnson, J.R., and 13 colleagues, 2006a. Spectrophotometric properties of materials observed by Pancam on the Mars Exploration Rovers: 1. Spirit. J. Geophys. Res. 111, doi:10.1029/2005JE002494.

Johnson, J.R., and 13 colleagues, 2006b. Spectrophotometric properties of materials observed by Pancam on the Mars Exploration Rovers: 2. Opportunity. J. Geophys. Res. 111, doi:10.1029/2006JE002762.

Kieffer, H.H., Martin, T.Z., Peterfreund, A.R., Jakosky, B.M., Miner, E.D., Palluconi, F.D., 1977. Thermal and albedo mapping of Mars during the Viking primary mission. J. Geophys. Res. 82, 4249–4291.

Kirk, R., Howington-Kraus, E., Redding, B., Galuszka, D., Hare, T.M., Archinal, B., Soderblom, L.A., Barrett, J., 2003. High-resolution topomapping of candidate MER landing sites with Mars Orbiter Camera narrow angle images. J. Geophys. Res. 108, doi:10.1029/2003JE002131.

Mangold, N., 2005. High latitude patterned grounds on Mars: Classification, distribution and climatic control. Icarus 174, 336–359.

Mark, D.M., Aronson, P.B., 1984. Scale-dependent fractal dimensions of topographic surfaces: An empirical investigation, with applications in geomorphology and computer mapping. Math. Geol. 16, 671–683.

McEwen, A.S., 1991. Photometric functions for photoclinometry and other applications. Icarus 92, 298–311.

Mellon, M.T., Jakosky, B.M., Kieffer, H.H., Christensen, P.R., 2000. High-resolution thermal inertia mapping from the Mars Global Surveyor Thermal Emission Spectrometer. Icarus 148, 437–455.

Muhleman, D.O., Butler, B.J., Grossman, A.W., Slade, M.A., 1991. Radar images of Mars. Science 253, 1508–1513.

Mushkin, A., Gillespie, A.R., 2006. Mapping sub-pixel surface roughness on Mars using high-resolution satellite image data. Geophys. Res. Lett. 33, doi:10.1029/2006GL027095.

Neumann, G.A., Abshire, J.B., Aharonson, O., Garvin, J.B., Sun, X., Zuber, M.T., 2003. Mars Orbiter Laser Altimeter pulse width measurements and footprint-scale roughness. Geophys. Res. Lett. 30, doi:10.1029/2002JE001849.

Putzig, N.E., Mellon, M.T., Kretke, K.A., Arvidson, R.E., 2005. Global thermal inertia and surface properties of Mars from the MGS mapping mission. Icarus 173, 325–341.

Shepard, M.K., Campbell, B.A., 1998. Shadows on a planetary surface and implications for photometric roughness. Icarus 134, 279–291.

Shepard, M.K., Brackett, R.A., Arvidson, R.E., 1995. Self-affine (fractal) topography: Surface parameterization and radar scattering. J. Geophys. Res. 100, 11709–11718.

Shepard, M.K., Campbell, B.A., Bulmer, M.H., Farr, T.G., Gaddis, L.R., Plaut, J.J., 2001. The roughness of natural terrain: A planetary and remote sensing perspective. J. Geophys. Res. 106, 32777–32796.

Shkuratov, Y., Starukhina, L., Hoffmann, H., Arnold, G., 1999. A model of spectral albedo of particulate surfaces: Implications for optical properties of the Moon. Icarus 137, 235–246.

Simpson, R.A., Harmon, J.K., Zisk, S.H., Thompson, T.W., Muhleman, D.O., 1992. Radar determination of Mars surface properties. In: Kieffer, H.H., Jakosky, B.M., Snyder, C.W., Matthews, M.S. (Eds.), Mars. Univ. of Arizona Press, Tucson, pp. 652–685.

Sinton, W.M., 1962. Temperatures on the lunar surface. In: Kopal, Z. (Ed.), Physicas and Astronomy of the Moon. Academic Press, New York, pp. 407–428.

Smith, B.G., 1967. Lunar surface roughness: Shadowing and thermal emission. J. Geophys. Res. 72, 4059–4067.

Spencer, J.R., 1990. A rough-surface thermophysical model for airless planets. Icarus 83, 27–38.

Titus, T.N., Kieffer, H.H., Christensen, P.R., 2003. Exposed water ice discovered near the south pole of Mars. Science 299, 1048–1051.

Wagner, R.J., 1967. Shadowing of randomly rough surfaces. Acoust. Soc. Am. J. 41, 138–147.

Wolff, M.J., Clancy, R.T., 2003. Constraints on the size of martian aerosols from Thermal Emission Spectrometer observations. J. Geophys. Res. 108, doi:10.1029/2003JE002057.

Wolff, M.J., and 12 colleagues, 2006. Constraints on dust aerosols from the Mars Exploration Rovers using MGS overflights and Mini-TES. J. Geophys. Res. 111, doi:10.1029/2006JE002786.